EFFECTS OF GEOMETRIC PARAMETERS AND FLOW ON MICROSWIMMER
MOTION IN CIRCULAR CHANNELS

by
ALPEREN ACEMOĞLU

Submitted to the Graduate School of Sabanci University
in partial fulfillment of the requirements for the degree of
Master of Science

SABANCI UNIVERSITY
SPRING 2014

EFFECTS OF GEOMETRIC PARAMETERS AND FLOW ON MICROSWIMMER
MOTION IN CIRCULAR CHANNELS

APPROVED BY:

Assoc. Prof. Serhat Yeşilyurt
(Dissertation Supervisor)

Assoc. Prof. Güllü Kızıltaş Şendur

Assoc. Prof. Ayhan Bozkurt

DATE OF APPROVAL   :   06.08.2014

...to my family

EFFECTS OF GEOMETRIC PARAMETERS AND FLOW ON MICROSWIMMER MOTION IN CIRCULAR CHANNELS

Alperen ACEMOĞLU
Mechatronics Engineering, MSc. Thesis, 2014
Thesis Supervisor: Assoc. Prof. Serhat YEŞİLYURT

ABSTRACT

Micro swimming robots offer many advantages in biomedical applications, such as delivering potent drugs to specific locations in targeted tissues and organs with limited side effects, conducting surgical operations with minimal damage to healthy tissues, treatment of clogged arteries, and collecting biological samples for diagnostic purposes. Reliable navigation techniques for microswimmers need to be developed for navigation, positioning and localization of robots inside the human body in future biomedical applications. In order to develop simple models to estimate trajectories of magnetically actuated microswimmers blood vessels and other conduits, effects of the channel wall must be understood well. In this thesis, experimental and numerical model results are presented on swimming of microswimmers with a magnetic head and a helical tail in laminar flows inside circular channels filled with glycerol. Designed to mimic the swimming behavior of biological organisms at low Reynolds number flows, the microswimmers are manufactured utilizing a 3D printer and a small magnet and consist of a helical tail and a body that encapsulates the magnet. The swimming motion results from the synchronized rotation of the artificial swimmer with the rotating magnetic field induced by three electromagnetic-coil pairs. In order to obtain linear and angular velocities and to analyze the motion of the microswimmer, a computational model is developed to obtain solutions of quasi-steady Stokes equations, which govern the swimming of the microswimmers and the flow inside the channel. Experiments and numerical simulations are carried out for a number of cases with different geometric parameters and flow rates in the channel. Numerical simulation results agree well with experimentally measured velocities of the swimmer validating the experimental results. It is also presented a discussion on the influence of geometric parameters of the tail, such as wavelength, amplitude and length, and the direction of rotation of the swimmer on its trajectory based on the observed behavior in experiments and numerical solutions. Moreover, a computational fluid dynamics (CFD) model for swimming of microorganisms with a single helical flagellum in circular channels is presented. The CFD model is developed to obtain numerical solutions of Stokes equations in three dimensions, validated with experiments reported in literature and used to analyze the effects of geometric parameters, such as the helical radius, wavelength, radii of the channel and the tail and the tail length on forward and lateral swimming velocities, rotation rates and the efficiency of the swimmer. Optimal shapes for the speed and the

power efficiency are reported. Effects of Brownian motion and electrostatic interactions are excluded to emphasize the role of hydrodynamic forces on lateral velocities and rotations on the trajectory of swimmers. For thin flagella, as the channel radius decreases, forward velocity and the power efficiency of the swimmer decreases as well; however, for thick flagella, there is an optimal radius of the channel that maximizes the velocity and the efficiency depending on other geometric parameters. Lateral motion of the swimmer is suppressed as the channel is constricted below a critical radius, for which the magnitude of the lateral velocity reaches a maximum. Results contribute significantly to the understanding of the swimming of bacteria in micro channels and capillary tubes.

SİLİNDİRİK KANALLARDA MİKROYÜZÜCÜ HAREKETİNE AKIŞIN VE GEOMETRİK PARAMETRELERİN ETKİSİ

Alperen ACEMOĞLU

Mekatronik Mühendisliği, Yüksek Lisans Tezi, 2014

Tez Danışmanı: Doç. Dr. Serhat YEŞİLYURT

Anahtar Kelimeler: Mikroyüzücüler, Mikroorganizmalar, Bakteri Hareketi, Düşük Reynolds Sayısında Yüzme, Hesaplamalı Akışkanlar Dinamiği, Silindirik Kanallarda Hareket

ÖZET

Mikroyüzücüler, hedeflenen organlara sınırlı yan etkilerle ilaç iletilmesi, canlı dokulara en az zararla cerrahi ameliyatların gerçekletirilmesi, kapalı damarların açılması, biyolojik dokuların teşhis amaçlı vücut içinden toplanması gibi biyomedikal uygulamalarda pek çok avantaja sahiptir. Gelecekteki biyomedikal uygulamalarda, yüzücülerin vücut içindeki pozisyonlarının kontrolü için güvenilir navigasyon teknikleri geliştirilmelidir. Manyetik olarak tahrik edilen yüzücülerin kan damarlarında yörüngelerini tahmin edebilmek için kanal duvarlarının etkileri iyi anlaşılmalıdır. Bu tez kapsamında, manyetik gövdeye ve helisel kuyruğa sahip gliserol ile doldurulmuş silindirik kanallarda dışarıdan manyetik alanla tahrik edilen mikroyüzücüler için sayısal ve deneysel çalışmalar yapılmıştır. Biyolojik mikroorganizma hareketlerini taklit eden yapay mikroyüzücüler için helisel kuyruklar 3 boyutlu yazıcılar ile üretilip üzerine manyetik gövde yerleştirilmiştir. Üretilen yapay yüzücüler, 3 çift elektromanyetik bobin ile tahrik edilmiştir. Yüzücünün lineer ve açısal hızlarını elde etmek için ve yüzücünün hareketini analiz etmek için Stokes denklemlerini çözen hesaplamalı bir model geliştirilmiştir. Farklı geometrik parametreler ve farklı akış hızları için deneysel ve simulasyonlar yapılmıştır. Elde edilen simulasyon sonuçları, deneysel sonuçları doğrulamaktadır. Ayrıca helisel kuyruğun dalga boyu, genliği ve uzunluğu gibi geometrik parametrelerin ve yüzme yönünün etkileri de deneysel ve sayısal çalışmalarla açıklanmıştır. Bunlara ek olarak, tek kuyruklu mikroorganizmaların düşük Reynolds sayılarında hareketleri hesaplamalı akışkanlar dinamiği ile modellenmiştir. Stokes denklemlerini çözen bu model literatürde yayınlanan deneysel çalışmalarla doğrulanmıştır. Kuyruk geometrisinin verimlilik ve lineer - açısal hızlar üzerindeki etkileri açıklanmıştır. Optimal mikroorganizma geometrisi ve simulasyonlardan elde edilen hızlar gösterilmiştir. Mikroorganizma yörüngeleri üzerindeki yatay ve açısal hızlara olan hidrodinamik etkileri vurgulamak için Brownian hareketi ve elektrostatik etkileşimler çalışmaya dahil edilmemiştir. İnce kuyruklu mikroorganizmalar için, kanal çapı azaltıldıkça, yüzme hızı ve verimliliği de azalmaktadır. Bununla beraber kalın kuyruklu mikroorganizmalar için yüzme hızını ve verimliliği maksimum yapan optimal bir kanal çapı vardır. Mikroorganizmanın yan yönlerdeki hareketi kanal çapı azaldıkça kısıtlanmaktadır. Elde edilen sonuçlar mikrokanallar ve kılcal tüpler içindeki bakteri hareketlerinin anlaşılmasına önemli katkılar yapmaktadır.

ACKNOWLEDGEMENTS

TABLE OF CONTENTS

LIST OF FIGURES

LIST OF TABLES

LIST OF SYMBOLS

B_0	Wave amplitude
D_{ch}	Diameter of the channel
D_h	Diameter of the cylindrical head
D_w	Wire diameter
D_{tail}	Tail diameter
f	Frequency
N_λ	Number of helical turns
L_h	Length of the cylindrical head
L_{ch}	Length of the channel
L_{sw}	Total length of microswimmer
L_t	Length of the tail
r	Equatorial radius of spheroid head
R_{ch}	Channel radius
R_{tail}	Tail radius
s	Polar radius of spheroid head
λ	Wave length of the tail

1   INTRODUCTION

Micro swimming robots can have a vast impact in development of new treatment methods for medical operations especially in minimally invasive surgery. Medical procedures such as targeted drug delivery, treatment of clogged arteries, marking damaged and cancerous tissues, visualization of aberrant body parts or organs will improve potentially and greatly with advances in the field. In order to control microswimmers inside conduits in the human body, such as arteries, lymphatic vessels and ureters, miniaturization of microswimmers and development of accurate external control mechanisms are essential. Furthermore, swimming of robots in confined environments must be well-understood to predict trajectories of robots in vessels, arteries and similar body conduits.

Propulsion mechanisms of microorganisms are widely adopted in development of artificial microswimmers for potential applications in medicine and biology such micro surgical operations, drug delivery and micro manipulations. Helical nanostructured propellers are controlled to follow the specified patterns [1]. Micro machines fabricated with 3-D laser writing are actuated with external magnetic field to perform transport cargo in fluid environments [2]. For real − time trajectory control of the swimmers, magnetic resonance imaging (MRI) is used to obtain feedback information [3].

The objective of the thesis is to make comprehensive explanation how geometric parameters of swimmer structure affect the swimming behavior since helical tail structure provides the propulsion. Fluid medium is also important; because swimmers show different characteristics in an unbounded fluid, near a plane wall and in channels. Here, swimmer behavior in circular channels is investigated for possible future biomedical applications in human blood vessels. Also swimmer behavior under constant flow is crucial to explain swimmer motion in blood streams. Microswimmer design that is used in experimental and numerical studies is inspired by singly flagellated natural microorganisms. Thus swimming of the natural organisms must be investigated for design of microswimmers. A number of studies in literature address the effects of

geometric parameters on the swimming of microorganisms near boundaries and in the bulk fluid [4, 5]. Further study is necessary to understand the swimming behavior of microorganisms in confinements such as circular channels.

This study will provide a basis for design of microswimmers by explaining the swimming velocity and the interactions with the channel walls. Designing microswimmers and developing the accurate control algorithm for swimmer motion, biomedical applications such as collecting biological samples from body and opening clogged arteries will be possible in the near future.

1.1   Background

1.1.1   Experiments

Magnetically actuated microswimmers are becoming increasingly popular due to compatibility of magnetic fields with medical procedures.   Dreyfus et al. [6] demonstrated a magnetic microswimmer made of a red blood cell, which serves as the body of the structure, and super paramagnetic particles that are coated with streptavidin and connected to each other with DNA molecules to form a filament that serves as the flagellum. Propulsion of the micro structure is demonstrated with the aid of an external magnetic field that induces undulatory motion of the flagellum. Swimming speed of such microswimmers depends on the frequency of oscillations and the length and elastic properties of flexible filaments [6].

Magnetic fields can be applied to actuate different propulsion mechanisms of microswimmers, such as, helical tails, oscillating flexible flagella or magnetic particles. Abbott et al. [7] report that microswimmers with helical tail and flexible flagella have better performance, i.e. more efficient and swims faster, compared to robots controlled directly with the magnetic field gradient. Microswimmers with helical tails can be controlled by adjusting the frequency of rotations and changing the direction of the external magnetic field [7].

In order to use microswimmers inside the human body, their sizes must be compatible with intended tasks. For example, micron sized robots are necessary for procedures inside capillary vessels, larger ones can be used in other conduits such as urethra and the ocular cavity. In a recent study, nano-structured magnetic swimmers are

manufactured and navigated on a desired trajectory [1]. SiO_2 propellers, whose dimensions are about 200-300 nm in diameter and 1-2 μm in length, are produced with shadow-growth method [1]. Zhang et al. [8] used micro manufacturing techniques to manufacture a helical artificial flagellum, which is about 47 μm in length and about 5 μm in diameter. Tottori et al. [2] used 3D lithography to manufacture polymeric helical structures about 35 μm in length and 6 μm in diameter and coated with ferromagnetic thin films on the surfaces. Rotations and translations of nano and micro structures are achieved with the rotational magnetic field [1, 2, 8].

Another approach to microswimmers in medical applications is modification of microorganisms with inorganic materials as demonstrated by Martel el al. [3]. Magnetotactic bacteria (MTB) can synthesize magnetic particles called magnetosomes, which allow controlling the bacteria magnetically. MTB based nano robots can propel themselves with two counter-clockwise rotating flagella. Velocity of nano robots is controlled with the effect of the external magnetic field on magnetosomes, manipulation of the temperature and interactions with the capillary wall [3].

There are a number of experiments on low Reynolds number flagellar swimming in circular channels filled with viscous oils and cm-sized swimmers. Honda et al. [9] used helical tails, which are rigidly connected to a cubic magnet, to demonstrate the effects of frequency, number of waves, diameter and total length of the helical tail on the swimming velocity of the structure inside a silicone-oil filled circular channel. Their results show that the forward speed of the swimmer increases with the frequency of the magnetic field and the total length of the helix, and reaches a maximum for the optimal value of number of waves [9]. Tabak et al. [10] conducted experiments with an autonomous swimmer that mimics the motion of eukaryotic microorganisms with the aid of a battery-powered DC motor, which is placed inside the body and used to rotate a rigid helical tail inside circular channels. An analytical model based on the resistive force theory, which is developed by Hancock [11, 12], is used to obtain the swimming velocity and compare with experiments. According to the results, swimming inside the narrow channel is slower than swimming inside the wide channel due to increased shear drag on the swimmer inside the narrow channel [10]. According to our previous experiments with a mm-long swimmer that consists a magnetic lump connected to a rigid helical tail, swimmer's velocity increases with the frequency up to the step-out frequency, for which the swimmer loses its synch with the rotating external magnetic

field with further increase in the frequency and slows down [13]. In addition, the CFD model shows that near-wall swimming is faster and more efficient than in-channel swimming [13].

Swimming of artificial structures and natural organisms has become increasingly popular and research has been widespread. A variety of structures that mimic the swimming mechanisms of microswimmers are constructed with different techniques such as a red blood cell with an artificial magnetic tail [6], a nanostructured helical propeller coated with ferromagnetic material [1], a soft magnetic metal square head and helical tail [8], a spherical magnetic head and helical tail [14]. Bacteria motion in confined geometries such as circular channels is examined by calculating motility coefficients [15], measuring the drift velocities [16] and measuring the chemotaxis parameters [17]. According to Berg and Turner [16], bacteria align with channel axis in confined geometries. Moreover, bacteria swim faster in restricted geometries, however further confinement leads to lower speeds [15].

Various bacteria follow helical trajectories during their motion such as magnetotactic bacteria [18]. In their experimental study, Zeile et al. [19] demonstrate that *Listeria monocytogenes* follow a right-handed helical trajectory which is also reported in an analytical study by Dickinson et al [20]. Crenshaw et al. [21] explain that *C. Reinhardtii* forms not only helical trajectories but also straight ones during forward motion; however *C. Reinhardtii* follows straight trajectories during backward motion. Moreover, according to the light intensity during phototaxis of bacteria, positive and negative orientations lead to a left and right − handed helical trajectories; which corresponds with a switch from negative to positive angular velocity [21].

Variety of stimuli such as concentration of repellents and attractants, temperature, magnetic field and light [22, 23] can induce bacterial locomotion, or motility, which may be exhibited not only in bulk fluids but also near solid surfaces and in confinements [15, 17, 24]. Brownian motion randomizes the direction and the position of the cell during a steady swimming period, and is coupled with hydrodynamic interactions to alter profoundly the trajectory of bacteria near a planar wall due to variations of the distance from the wall [25]. However, swimming behavior of bacteria in confinements exhibits nearly steady behavior [15]. Electrostatic and van der Waals forces are effective and cause adhesion only when the bacteria are very close to the boundary about 10 nm [15].

As demonstrated in previous works, e.g. [4,5] , the swimming characteristics of bacteria with helical tails are vital to understand phenomena such as surface accumulation and mobility in bulk fluids and in porous media. DiLuzio et al. [26] studied the swimming behavior of *E. coli* cells in confined geometries, reported that bacteria swim close to porous agar surface than solid PDMS surface, and showed that the motion of cells is affected by the guide material in narrow channels; the percentage of the cells swimming close to the agar surface decreases as the channel height increases, indicating that hydrodynamic interactions diminish [26]. In an experimental study with mammalian sperm cells and unicellular green algae, Kantsler et al. [27] demonstrated that flagella-surface interactions are mostly important on the surface scattering mechanism of cells.

Biondi et al. [15] conducted experiments to determine the effects of restricted geometries on the swimming behavior of *E. coli* in micro channels with heights varying from 2 to 20 μm, calculated the motility coefficients from the single-cell data, and reported that swimming behavior remains nearly constant in confined geometries. Maximum swimming speed is achieved in the 3-μm channel, but the speed decreases because of increasing drag force due to the restriction in the 2-μm channel [15]. Berg and Turner [16] conducted experiments with motile and non-motile bacteria in capillaries of 10 μm and 50 μm in diameter, reported that drift velocities and diffusion coefficients are higher in 10-μm capillary than in 50-μm, and concluded that bacteria align with the channel's longitudinal axis in restricted geometries. Liu et al. [17] performed experiments with *E. coli* in a capillary tube with 50 μm diameter, developed a method to measure chemotaxis parameters at the single cell level, demonstrated that the swimming speed has a normal distribution, and concluded that there is an optimal viscosity which maximizes the swimming speed [17]. Furthermore, authors also obtained the distribution of turn angles, which exhibits a non-normal behavior due to geometric restriction [17]. Mannik et al. [28] studied the motility of *E.coli* inside micro channels with diameter about 2 μm and narrower, which are marginally larger, about 30%, than the diameter of the cells. Authors showed that bacterial motion is one-dimensional due to shallowness of the channel and the bacterium swims at the same average speed in the channels with diameters larger than 1.1 μm as in the chamber. The motility of the bacteria vanishes in smaller channels with diameter 0.8 μm and smaller, but the bacteria can still pass through these channels by growth and division.

1.1.2 Computational and Theoretical Modeling

In addition to experimental work, analytical and computational models are reported in literature; computational models are based on computational fluid dynamics (CFD) and boundary element methods (BEM). In [29], an analytical model of a bio-inspired microswimmer with a flexible tail based on the resistive force theory (RFT) is developed to predict the trajectory of the microswimmer; analytical model results agree well with CFD model results. In [30], a three-dimensional CFD model is developed for the microswimmer with a spherical magnetic head attached to a helical tail; comparisons are made between unbounded, in-center and near-wall swimming inside a cylindrical channel. Results show that swimming near the channel wall is faster and more efficient than swimming in the center, the efficiency of the robot is frequency-independent, and forces perpendicular to the axis of the swimmer, which aligns with the axis of the channel, are very much higher for near-wall swimming than in-center swimming [30].

Using the BEM method, Ramia et al. [31] studied swimming of microorganisms with spherical bodies and rotating helical flagella for four different cases: in an unbounded medium, near a plane boundary, midway between two parallel boundaries and with other swimmers nearby. Swimming speed and angular velocity of the swimmer in an unbounded fluid are compared to the planar boundary case, a decrease less than 10% due to the flagellar locomotion is observed. The interaction with other neighbor swimmers or parallel planar boundaries causes a decrease in the velocity as much as 10% [31]. In a similar study, a BEM model is used to study forward and backward motion of flagellated bacteria close to a planar boundary [32]. It is demonstrated that trajectories and swimming speeds are different during forward and backward motions of the swimmer owing to effects of the pitch angle and the angle between the boundary and the axis of the helical tail [32]. Giacche et al [33] used a BEM model to study the entrapment of microorganisms with helical tails near planar walls, according to results the numerical model agrees very well with experimental observations, and the helical wavelength and amplitude have a profound effect on the stable trajectory of the microorganism.

Recently, Felderhof [34] developed an analytical model for swimming of infinite helices inside circular channels based on first order expansion for the geometry of the

helical structure. According to results, in-channel swimming is faster and more efficient than unbounded swimming especially for thick tails.

Moreover, theoretical models, such as the resistive force theory (RFT) [12] and slender-body theory [35] and computational solutions of Stokes equations, such as the boundary element method [36], are developed to obtain swimming velocities near plane boundaries [4, 37] and in bulk fluids [38]. Keaveny et al. [39] developed a numerical model to analyze the spiral motion of a swimmer with a flexible tail composed of magnetic spheres attached with filaments and actuated by an external magnetic field. In our earlier work [30, 40], behavior of microswimmers with a magnetic head and a helical tail is studied with quasi-steady numerical solutions to Stokes equations in order to identify the effect of geometric parameters of the swimmer on the forward and lateral velocities and wobbling rates.

Controllable swimming inside channels in the presence of a Poiseuille flow bears importance for manipulating the motion of artificial and natural organisms in blood vessels. In a recent study, Zöttl and Stark [41] achieved non-linear dynamics of a spherical microswimmer in the Poiseuille flow. Trajectories of a spherical microswimmer are presented by discussing the swinging and tumbling motion of the swimmer. Authors also reported that confinement leads to more stable trajectories [41]. The motion of a spherical microswimmer in cylindrical Poiseuille flow is examined to determine chaotic dynamics [42]. It is reported that regular or chaotic motion of a swimmer depends on small finite periodic oscillations which vary with the position and orientation of the swimmer in the channel and efficient upstream (downstream) swimming takes place at (away from) the center [42]. It is also reported that African trypanosome cells which are subjected to flow, form an oscillatory path similar to a sinusoidal wave as they subjected to flow in bounded geometries [43]. Surface accumulation characteristics of bacteria in the absence and presence of the external flow in confined geometries are presented by changing the parameters such as cell density, channel diameter and the flow velocity; according to results, steady flow leads to accumulation of bacteria near channel wall [44].

Effects of other forces than Stokes drag are of particular interest for oscillatory motion of microswimmers. Wang and Ardekani [45] report that unsteady effects such as the Basset - history and added-mass may play an important role in addition to Stokes drag force in low Reynolds number swimming of microorganisms when the frequency of oscillations are substantially large. In fact, unsteady history and added-mass forces

may exceed the value quasi-steady Stokes drag when the product of Strouhal, Sl, and Reynolds, Re, numbers is much greater than one, i.e. $SlRe = \rho fD/\mu \gg 1$, typically when the frequency of oscillations, f, is very large, roughly in the kHz range for microswimmers [45].

Reynolds number of the bacterial locomotion is very low, about 10^{-5}, and the flow is governed by incompressible Stokes equations. Felderhof [34] constructed an approximate solution based on perturbation methods for infinitely long 'thick' helical filaments rotating and moving axially inside circular channels, and showed that the confinement leads to increased swimming speed and efficiency depending on the stroke parameters such as the amplitude, wavelength and the relative radius of the filament with respect to the channel radius.

Boundary element method (BEM) is used in numerical models of swimming of microorganisms in the bulk fluid, e.g. [5, 36], near planar walls, e.g. [4, 31], and recently in channels [46]. Zhu et al. [46] modeled the locomotion of ciliated microorganisms with a spherical squirmer model inside straight and curved capillary tubes with a BEM model, which is tuned for geometric confinements. Authors reported that the confinement and near-wall swimming always decrease the swimming speed of the squirmer with tangential surface deformation, but improve the speed of the squirmer with normal surface deformation, which pushes against the wall [46].

Numerical solutions to Stokes equations, such as finite-element-method (FEM) based computational fluid dynamic (CFD) models are powerful tools to study effects of the proximity to solid surfaces on the swimming behavior of bacteria and to identify hydrodynamic interactions between the surface and the cell. Temel and Yesilyurt [30] used a three-dimensional CFD model for an actual artificial swimmer used in experiments to study the effect of distance from the wall and the geometry of the helical tail on the swimming speed and the power efficiency, which attain maximum values at a critical distance from the wall compared to center swimming.

1.2   Scope of the Thesis

The scope of the thesis is to understand the effects of the geometric parameters such as wavelength and amplitude of the helical tail, length and diameter of the cylindrical head, the radial position of the swimmer, and channel size and effects of the

channel flow on the behavior of artificial swimmers and organisms by in-channel experiments with swimmers manufactured by 3D printers and use of steady-snapshot solutions of Stokes equations. Although there are a number of studies on spherical swimmers in Poiseuille flow, the motion of swimmers with a helical tail and a magnetic head needs to be understood well.

For experiments, tail geometries of the swimmers are manufactured utilizing 3D printers and permanent magnets are placed on top of them. Swimmers are rotated by means of an external rotating magnetic field, which is generated by Helmholtz coil pairs and perpendicular to the channels axis and to the magnetization vector of the radially magnetized cylindrical head. Experiments are conducted with a number of swimmers having different dimensions and helical parameters in channels with three different diameters. In addition to the helix and the tail length, channel radius is also varied in experiments to study the effect of the flow restriction on the swimming performance.

In the simulations, swimmers with a rigid helical tail and a magnetic head are examined in Poiseuille flows inside circular channels filled with highly viscous fluid, glycerol, to ensure low Reynolds number micro flow conditions. Linear and angular velocities of swimmers are obtained by using force-free and torque-free conditions. No-slip boundary conditions are applied to the channel wall. On swimmer surface no-slip boundary conditions are expressed as moving wall boundary conditions. For microorganisms, the numerical model is validated against experimental work reported in literature; for microswimmers, the numerical model is validated with experiments and used for other cases that are not covered in the experiments such as the effects of the radial position on the swimming speed.

Understanding motion of artificial and natural swimmers in confinements is significant in order to use the swimmers in blood vessel for biomedical applications. The effects of the geometrical parameters microorganisms swim at low Reynolds numbers are also important; Martel et al. [3] think that natural organisms can be used as robots in human microvasculature. This thesis will provide a basis for design of the microswimmers to be used in future biomedical applications such as drug delivery, opening clogged arteries.

2   METHODOLOGY

2.1   Experiments

2.1.1   Fabrication of Microswimmers

Microswimmers consist of a permanent magnetic cylindrical head and a helical tail manufactured with a 3D-printer (Projet HD 3000) which uses VisiJet EX 200 polymers. 3D-printing technology offers design flexibility and allows setting the values for the tail length and the wavelength of a tail as desired. Radially polarized neodymium-iron-boron ($Nd_2Fe_{14}B$) cylindrical permanent magnets, which are 0.4 mm in diameter and 1.5 mm in length, are placed between the holders at the tip of the helical tail as the head of the swimmer with a strong adhesive (Figure 2.1).
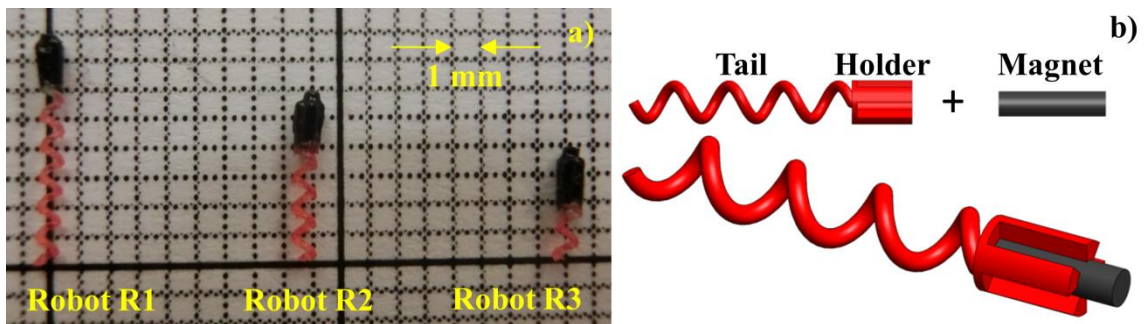
Figure 2.1   a) Sample swimmer structures with magnetic head (black) and helical tail (red) that manufactured with 3D printer. b) Schematic presentation of manufacturing process of swimmers.

2.1.2   Experimental Setup

Swimmers are placed axially in cylindrical glass tubes with diameters varying between 1.6 and 4.8 mm and 10 cm in length and filled with glycerol whose viscosity is μ = 1.412 Pa·s, and density is ρ = 1261 kg/m^3. The helical axis of the swimmer is

aligned with the axis of the channel. Channel's inlet is connected to a syringe pump by means of a flexible tube (see Figure 2.2 and Figure 2.3).
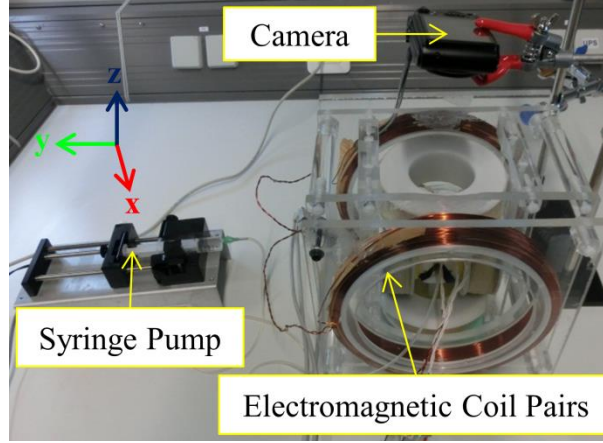
Figure 2.2 Experimental setup with syringe pump, electromagnetic coil pairs and camera.

Three pairs of Helmholtz coils are placed in **x-**, **y-** and **z-** directions to obtain a uniform magnetic field around the channel, which lies in the **x-** direction, as previously demonstrated for bulk swimming of artificial swimmers in literature, e.g. [8]. In this study, out-of-phase low frequency AC currents are applied to two coil-pairs in **y-** and **z-** directions to obtain a magnetic field that rotates in the **x-** direction on **y-z** plane.

The magnetization vector, **m**, of the permanent magnet also lies on the **y-z** plane having an angle θ with the magnetic field vector. The torque on the magnetic head of the swimmer is calculated from the cross product of the magnetic dipole moment of the permanent magnet and the magnetic induction of the coils, **B**. For a magnetic field that rotates in the clock-wise direction with angular frequency ω, the magnetic torque is obtained as follows:

$$\tau_{M} = \mathbf{m} \times \mathbf{B} = \mu_0 \mathbf{m} \times \mathbf{H} = \mu_0 m_0 H_0 \begin{bmatrix} 0 \\ \sin(\omega t + \theta) \\ \cos(\omega t + \theta) \end{bmatrix} \times \begin{bmatrix} 0 \\ \sin(\omega t) \\ \cos(\omega t) \end{bmatrix} = \mu_0 m_0 H_0 \begin{bmatrix} \sin\theta \\ 0 \\ 0 \end{bmatrix} \qquad (1.1)$$

where μ_0 is permeability of the free space and **H** is the magnetic field vector. The magnetic dipole moment of the cylindrical head, **m**, can be obtained by multiplying the volume of the magnet, ϑ, and magnetization of the material, **M**.

$$\mathbf{m} = \mathbf{M}\vartheta \qquad (1.2)$$

For synchronous rotation of the swimmer with the magnetic field, magnetic torque must be larger in magnitude than the viscous torque on the swimmer. The angle θ

between the magnetic field vector and the magnetic dipole varies according to the balance between the magnitudes of the magnetic and viscous torques. For large magnetic fields rotating at slow rates the angle is very small, and at step-out frequency when the swimmer barely keeps up with the rotation of the magnetic field the angle is $\pi/2$.
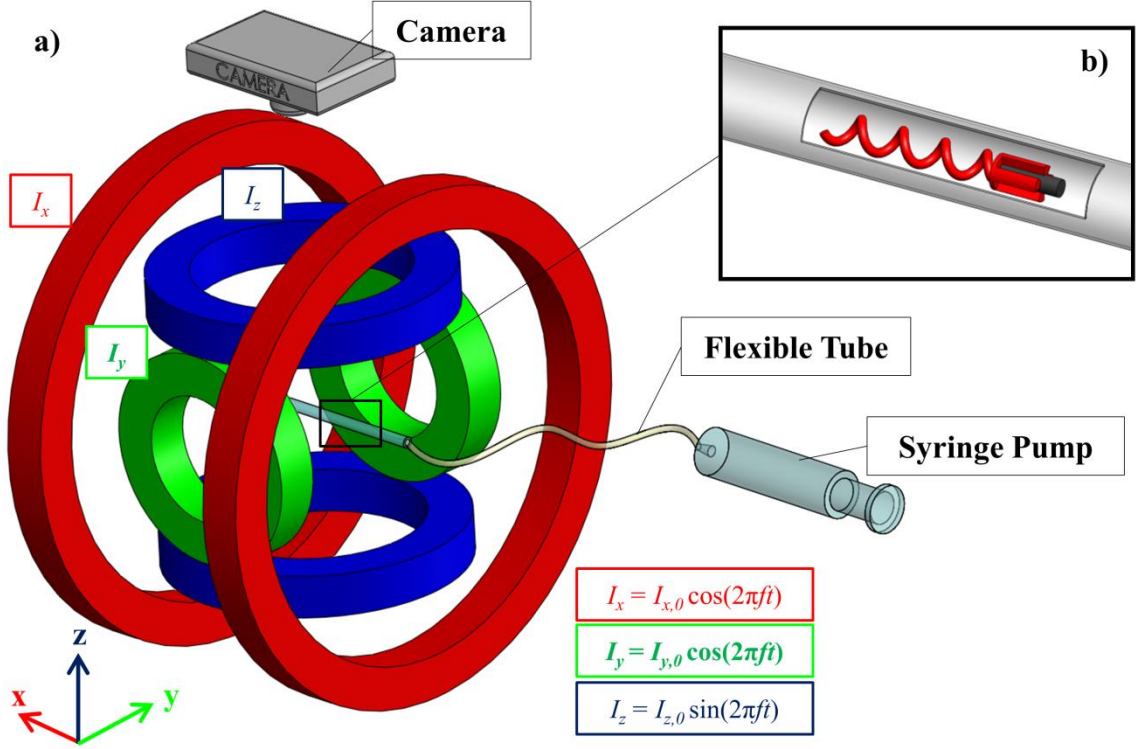
Figure 2.3 a) Schematic presentation of experimental setup which consists electromagnetic coil pairs, syringe pump, flexible tube, circular channel and camera. b) Close-up to circular channel to demonstrate the microswimmer inside the channel with partial section view.

The magnetic field strength to obtained required torque depends on the current (I), number of turns (N), radius of the coil (a), the vertical distance between magnet and the center of the coil (x). The magnetic field strength for the coil consists of one-turn wire, the current I, in the distance x from the center of the coil is calculated as:

$$H = \frac{Ia^2}{2(a^2 + x^2)^{3/2}} \tag{1.3}$$

The distance between the coil pairs must be equal to radius of the coils according to Helmholtz coil pair rule. Thus magnetic induction magnitude for coil pairs with radius R, and consist N-turn can be calculated as:

$$B = \mu_0 H = \left(\frac{4}{5}\right)^{\frac{3}{2}} \frac{\mu_0 N I}{R} \qquad (1.4)$$

According to (1.1), when the swimmer is not aligned with the axis of the channel, magnetization in the **x-** direction is no longer zero, and the magnetic torque on the swimmer has non-zero components in **y-** and **z-** directions as well. This may play an important role in the stability of the swimmer's trajectory as discussed in the results section here.

Uniform rotating magnetic field is obtained by adjusting the AC current on electromagnetic coils by means of Maxon ADS_E 50/5 motor drives and NI DAQ hardware. The frequency and the magnitude of the current are set via LabView software. In order to get a rotating magnetic field, alternating current must be applied with a phase shift. For example, current applied to small and big coils can be expressed as follows: $I_{small\_coil} = I_{0,\ small\_coil} \sin(2\pi f t)$ and $I_{big\_coil} = I_{0,\ big\_coil} \cos(2\pi f t)$. Forward and backward swimming can be obtained by using two coil pairs. Third coil pair is used for navigation by changing the direction of the magnetic field vector. Here, forward and backward motion is investigated in the straight circular channels. Frequencies of the current for each coil is same ($f_x = f_y = f_z$) whereas the current magnitudes are different ($I_x \neq I_y \neq I_z$); because orthogonal coils pairs have different dimensions, in order to obtain uniform magnetic field in the middle of the setup, current magnitudes must be different for equal magnetic field strengths ($B_x = B_y = B_z$).

The motion of the swimmer is recorded with the CASIO EX-ZR1000 digital camera at 120 frames per second. Trajectory of the swimmer and components of the velocity vector are obtained by image processing tools in MATLAB (APPENDIX).

2.2   Computational Model

2.2.1   Approach

The microswimmer that consists of a cylindrical magnetic head and a rigid left-handed helical tail is placed inside a circular channel as shown in Figure 2.4. Inlet and outlet of the glycerol-filled channel are closed. The cylindrical magnet is placed inside the left-handed helix starting from the top as shown in Figure 2.4. Geometric dimensions used in the model based on our experiments are presented in Table 2.1.

Non-dimensional values are obtained from the normalization based on the diameter of cylindrical body.

Circular channel that contains the swimmer is filled with glycerol, which has a dynamic viscosity of 1.412 Pa-s. Reynolds number is based on the swimmer's diameter as the length scale and the tangential velocity of the head as the velocity scale, and given by:

$$\text{Re} = \frac{\rho V D}{\mu} = \frac{\rho \omega_x D_h^2}{2\mu} \tag{1.5}$$

where $\omega_x = 2\pi f$ is the angular velocity of swimmer in the **x**-direction (see Figure 2.4), ρ is the fluid density, μ is the dynamic viscosity of fluid and D_h is the diameter of the cylindrical head of the microswimmer (see Figure 2.4). When the rotation frequency is set to 1 Hz, the Reynolds number is $4.51 \times 10^{-4} \ll 1$ where viscous forces are dominant to inertial forces.
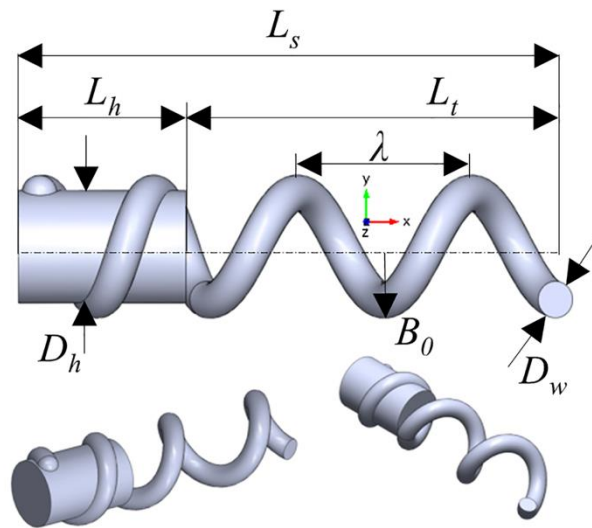
Figure 2.4 Geometric parameters, coordinate axes and front and back isometric views of the microswimmer.

The angular velocity of the swimmer in the **x**-direction, which is the axis of the swimmer (Figure 2.4), is effectively equal to the angular velocity of the rotating magnetic field in the same direction. As long as the magnetic moment is sufficiently high to overcome the viscous torque, rotation of the swimmer will be in-synch with the rotation of the magnetic field up to the step-out frequency as reported previously in [1, 8, 13].

The flow field in the channel has a very low Reynolds number and is governed by Stokes equations:

$$\mu \nabla^2 \mathbf{u} - \nabla p = 0, \quad \nabla \cdot \mathbf{u} = 0 \tag{1.6}$$

where μ is viscosity, $\mathbf{u}$ is the velocity vector and p is the pressure.

The centerline of the left-handed helical tail is given by:

$$\mathbf{P}_h = \left[x_h, B_0 \sin(kx_h + \varphi), B_0 \cos(kx_h + \varphi) \right] \tag{1.7}$$

where x_h is the **x**-coordinate, k is wave number ($k = 2\pi/\lambda$), $\varphi = \omega t$, is phase angle, and B_0 is the wave amplitude, or the radius of the helical tail, which is also the radius of the cylindrical head.

Linear velocities of the rigid-body swimmer in **x**, **y** and **z**- directions, i.e. U_{sw}, V_{sw} and W_{sw}, and angular velocities in **y** and **z**-directions, i.e. ω_y and ω_z, are 5 unknowns, which need to be determined by 5 additional equations. The angular velocity in the **x**-direction, ω_x, is an input. Force-free swimming conditions in **x**, **y** and **z**- directions provide three equations for the linear velocity vector of the rigid swimmer, and expressed by setting the total fluid forces at the surface of the swimmer to zero. Net fluid force is calculated by integrating the fluid stresses on the swimmer surface and set to zero:

$$F_j = \int_{S_{swimmer}} \sigma_j \cdot \mathbf{n}_s dS = 0 \tag{1.8}$$

where $j = \{x, y, z\}$ indicates the direction, σ is the fluid stress tensor, and $\mathbf{n}_s$ is the surface normal vector. Similarly to force-free swimming conditions, torque-free swimming conditions are used to obtain angular velocities in **y** and **z**- directions:

$$\tau_y = \int_{S_{swimmer}} \left[(z - z_{com})\sigma_x - (x - x_{com})\sigma_z \right] \mathbf{n}_s dS = 0 \tag{1.9}$$

$$\tau_z = \int_{S_{swimmer}} \left[(x - x_{com})\sigma_y - (y - y_{com})\sigma_x \right] \mathbf{n}_s dS = 0 \tag{1.10}$$

where x, y, z are the coordinates of the position vector on the surface of microswimmer and $(x, y, z)_{com}$ are the coordinates of the center of mass.

The angular velocity component in the **x**-direction, ω_x, coincides with the channel's axis, and taken as a constant input assuming that the swimmer's rotation is synchronized with the rotation of the external magnetic field. Alternatively, magnetic torque in the **x**- direction can be used as an external torque constraint for the viscous torque in this direction. However, as long as the magnetic torque is large enough to

overcome the viscous torque, swimmer's rotation in the **x**- direction is synchronized with the magnetic field as observed in experiments here and in literature [1,8,13]. Only for frequencies larger than the step-out frequency [8], swimmer cannot rotate in synch with the magnetic field when the magnetic field is not strong enough, but synchronized motion can be restored by increasing the intensity of the field [8,13]. Here, we are interested in the effect of geometric parameters in the swimming performance assuming that the magnetic field strength can be set to a value high enough to sustain synchronized swimming, and used a kinematic constraint for the angular velocity component, $\omega_x = 2\pi f$. Furthermore, in simulations, frequency, f, is set to unity as a unit scale, since all velocities scale linearly with the frequency.
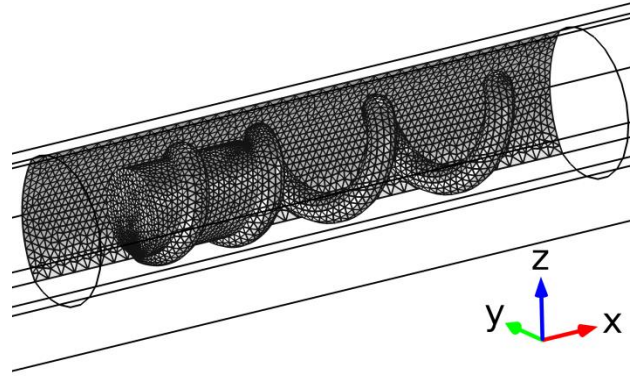
Figure 2.5 A representation of the finite-element mesh distribution over the surface of the microswimmer and the portion of the wall near the swimmer.

Table 2.1   Geometric parameters of the model

Symbol	Description	Base Values	Dimensionless values
D_h	Diameter of the cylindrical head	400 μm	1
L_h	Length of the cylindrical head	600 μm	1.500
λ	Wave length of the tail	625 μm	1.5625
B_0	Wave amplitude	200 μm	0.5
L_t	Length of the tail	1250 μm	3.125
D_w	Wire diameter	130 μm	0.325
L_{sw}	Total length of microswimmer	1850 μm	4.625
D_{ch}	Diameter of the channel	1000 μm	2.5
L_{ch}	Length of the channel	6000 μm	15
N_λ	Number of waves	2	2
f	Frequency	1[Hz]	1[Hz]

At closed inlet and outlet of the channel and on the channel wall, no-slip boundary condition is used:

$$\mathbf{u} = 0 \quad \text{at} \quad x = 0, L_{ch} \text{ and at } r = R_{ch} \tag{1.11}$$

16

No-slip boundary conditions at the surface of the swimmer are expressed as moving wall conditions, for which the linear and angular velocity vectors of the swimmer are used to calculate the local velocity of the swimmer's moving boundary:

$$\mathbf{u} = \begin{bmatrix} U_{sw} \\ V_{sw} \\ W_{sw} \end{bmatrix} + \begin{bmatrix} \omega_x \\ \omega_y \\ \omega_z \end{bmatrix} \times \begin{bmatrix} x - x_{com} \\ y - y_{com} \\ z - z_{com} \end{bmatrix} \quad (1.12)$$

2.2.1.1 Microorganisms

The monotrichous bacteria model used in [4] and shown in Figure 2.6 is taken as the model organism here and placed at the centerline of the circular channel. Since head and tail of microorganisms are rotating inversely, the differences in numerical model are presented for natural organisms.
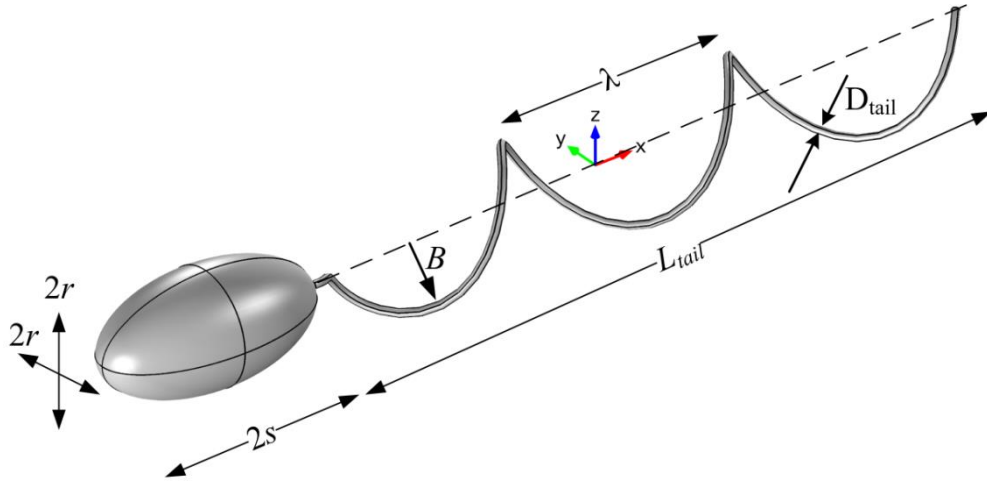
Figure 2.6 Parameters of the cell geometry; description of the parameters are shown in Table 2.2.

The helical tail is attached to the cell body with a simple joint as shown in Figure 2.6 and rotates in the opposite direction to the rotation of the body. The helical tail is modified with the amplitude growth rate as proposed in [38]. The centerline of the left-handed helical tail is given by:

$$X(\xi) = \left[\xi, B(1 - e^{k_E^2 \xi^2}) \sin(k\xi - \varphi), B(1 - e^{k_E^2 \xi^2}) \cos(k\xi - \varphi) \right] \quad (1.13)$$

where ξ is the **x**- coordinate, k is wave number ($k = 2\pi/\lambda$), φ is phase angle that corresponds to the angular position of the tail during its rotation, i.e. $\varphi = \omega t$, B is the

wave amplitude, which is set to equatorial radius of the spheroid head, r, and k_E is the growth rate of the amplitude. Phan-Thien et al. [36] and Shum et al. [4] studied similar geometry of the bacterium as well.

No-slip boundary conditions on the surface of the organism are expressed as moving wall conditions. Local velocities of the head and the tail of the organism are calculated using angular, $\mathbf{\Omega}$, and linear velocities, $\mathbf{U_{sw}}$, as follows:

$$\mathbf{u}_{head} = \mathbf{U_{sw}} + \mathbf{\Omega} \times (\mathbf{x} - \mathbf{x_{com}}),$$

$$\mathbf{u}_{tail} = \mathbf{U_{sw}} + \begin{bmatrix} \omega & \Omega_y & \Omega_z \end{bmatrix}' \times (\mathbf{x} - \mathbf{x_{com}})$$

(1.14)

where ω is the angular velocity of the tail with respect to fixed coordinate frame in the $\mathbf{x}$-direction, subscript 'com' represents the center of mass of the bacterium and $[]'$ represents transpose of the vector. The actual center of mass is very close to the midpoint of the spheroid head since the tail is very thin. For the base case bacterium model with $\lambda/s = 3$ and $L/s = 6$, the distance between the center of the spheroid head and the center of mass is about $s/10$.

Table 2.2   Geometric parameters of the model organism

Symbol	Decription
s	Polar radius of spheroid head
r	Equatorial radius of spheroid head
λ	Wavelength of the tail
N_λ	Number of helical turns
B	Wave amplitude
L	Length of the tail
R_{tail}	Tail radius
D_{tail}	Tail diameter
f	Frequency
R_{ch}	Channel radius
L_{ch}	Channel length

Swimming efficiency, η, is calculated from the ratio of the rate of work done to propel the organism in the forward direction to the rate of work done to rotate the helical tail with respect to the body of the organism as commonly used in literature, e.g. [47]:

$$\eta = \frac{F_{body} U_{sw}}{\tau_{tail} (\Omega_x + \omega)}$$

(1.15)

where F_{body} is the drag force on the body, which is calculated by integrating the fluid stresses, U_{sw} is the forward velocity (in the axial direction of the channel), τ_{tail} is the tail torque, Ω_x is the angular velocity of the body and ω is the angular velocity of the tail about **x**-axis.

2.2.2 Numerical Model

Equations (1.6), (1.8)-(1.10) are subject to boundary conditions (1.11) and (1.12) and solved numerically with the finite-element method using the commercial software COMSOL Multiphysics [58]. The model has approximately 150K elements, mostly tetrahedral, and 1.1M degrees of freedom. P1+P1 elements are used as discretization of fluids. Solver of the model is chosen as PARDISO in all simulations. On the swimmer surface triangular elements are used. Surface of the microswimmer and part of the channel wall close to the swimmer have finer mesh quality than other parts of the channel away from the swimmer (Figure 2.5). In order to improve the accuracy of the solution in near-wall simulations, boundary layer mesh that consists of five layers of prism elements are used between the swimmer and the channel wall.

Convergence of the finite-element mesh is tested by varying the number of elements. For each case there are five boundary layers between the swimmer and the channel wall. As the mesh size decreases on the surface of the swimmer, number of elements and degrees of freedom increase (Table 2.3). Solution with the finest mesh requires 97 GB of RAM which is the maximum available memory in the workstation used for the simulations. Error rates of linear velocities are calculated according to the simulation with the finest mesh. Maximum error in the results with the mesh used in the simulations is less than 2%.

Table 2.3   Convergence results and errors based on the finest mesh for different number of elements

Number of elements (x10^3)	Degrees of Freedom (x10^6)	System Memory (GB)	Error in U_{sw} [%]	Error in V_{sw} [%]	Error in W_{sw} [%]
150	1.140	52	0.37	1.96	0.42
172	1.305	61	0.29	2.96	0.22
210	1.587	80	0.11	0.98	0.05
226	1.700	87	0.11	1.13	0.13
248	1.860	97	0*	0*	0*
* Error rate of solution with finest mesh is accepted **0** and the other error rates are calculated according to these results.					

3 EFFECTS OF GEOMETRIC PARAMETERS ON THE SWIMMING OF NATURAL ORGANISMS

The CFD model of the bacterial locomotion is validated against the results reported by Goto el al. [5], who developed a boundary-element-method (BEM) model and conducted experiments with individual species of *V. algino* to study swimming velocity and body rotation rates, which are computed with the CFD model here based on the geometric parameters of cells reported in [5] and for a channel with radius 15 μm and length 40 μm, which is sufficiently larger than the average diameter of the cell body and the average length of the cell. Calculated and reported ratios of the swimming velocity to the body rotation rate are shown in Figure 3.1. The CFD model results are almost identical with the BEM model results and very close to the measured ones.
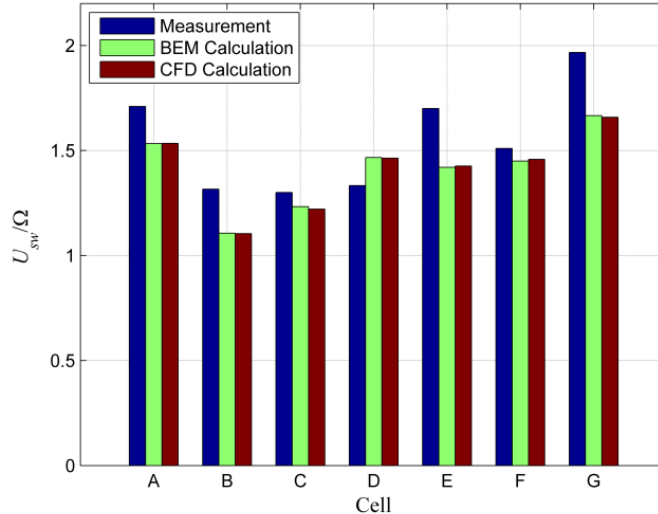
Figure 3.1 Ratio of the swimming velocity and the body rotation rate: measurements (blue) and BEM calculations (green) reported in Goto et al. [5], CFD results (red) for V. algino species reported in Goto et al. [5] and labeled A to G.

In addition to the forward velocity, torques generated by the flagellar motor are computed with the CFD model and compared to the BEM results reported in [5] as shown in Figure 3.2 a. Values of the flagellar torque from the CFD model are slightly higher than the ones from the BEM model. In order to find out if the presence of the

channel in CFD simulations may have an effect, we calculated the flagellar torque for different channel radii as shown in Figure 3.2 b. The flagellar torque rapidly decreases with increasing channel radius for narrow channels, but for large radii flagellar torque does not vary with the channel radius significantly. Thus, the channel radius can be deemed sufficiently large. Comparisons with results in [5] indicate that there is about 10% difference between the calculated ones here and the reported results.
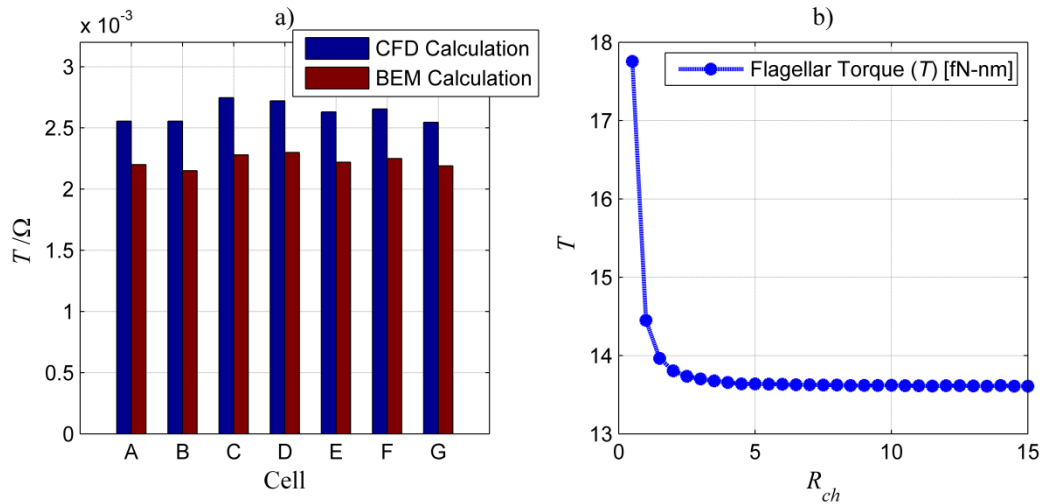
Figure 3.2 Flagellar torque normalized by the body rotation rate, T/Ω [pN-mm-s]. (a) CFD calculations (blue), BEM calculations (red) reported by Goto et al. [5]. (b) Effect of the channel radius, R_{ch} [μm], on the flagellar torque, T [fN-nm]

3.1   Forward Velocity

Performance metrics of the flagellar swimming, such as the forward velocity, power efficiency and the magnitude of lateral velocities vary with geometric parameters of the tail. In the simulations, the radii of the spheroid body in long and short axes are fixed as reference length scales, $s = 2r = 1.11$ μm, and the tail rotation frequency is set to unity. Radius of the sphere which has the same volume as the spheroid head, a, is 0.7 μm as also adopted in [4]. Tail envelop growth rate which defines the part of tail where it is connected to the spheroid head is taken as $k_E = 2\pi/s$.

Inside wide channels, there is a slight improvement in the stroke, which is the distance traveled during a full rotation of the tail, for larger wavelengths especially for shorter tails than inside narrow channels. Shum et al. [4] studied the forward velocity of the cell with the same dimensions near a planar wall, and showed that forward velocity reaches its maximum when there is about one full wave on the tail, i.e. for $N_\lambda = 1$. Here,

21

the forward velocity becomes maximum for N_λ values between 2 and 3. Lastly, the forward velocity exhibits similar dependence on the tail length and the wavelength in narrow and wide channels with slightly varying loci of the optimum (see the black circles in Figure 3.3a for $R_{ch}/r = 3$ and Figure 3.3b for $R_{ch}/r = 13.5$). Stroke values are slightly larger for swimming inside the wide channel than the ones inside the narrow channel.
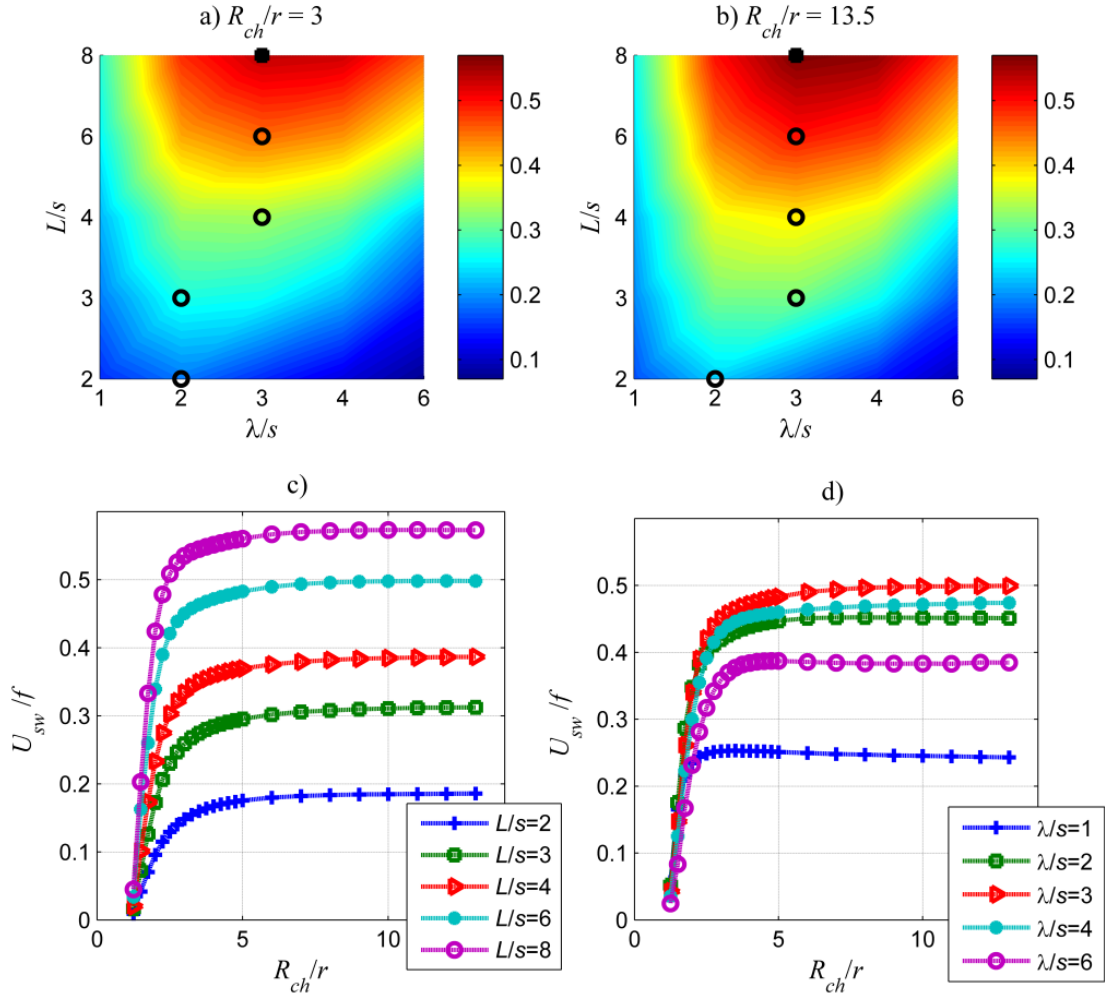
Figure 3.3 Surface plot of the stroke, U_{sw}/f [μm], as a function of the wavelength and the length of the tail for (a) narrow channel ($R_{ch}/r = 3$) and (b) wide channel ($R_{ch}/r = 13.5$). Black circles represent the loci of maximum values of the stroke for each tail length. Solid squares represent the maximum values for all computations. (c) U_{sw}/f [μm] as a function of the normalized channel radius, R_{ch}/r, for different tail lengths and the fixed wavelength ($\lambda/s = 3$). (d) U_{sw}/f [μm] as a function of the channel radius, R_{ch}/r, for different wavelengths and the fixed tail length ($L/s = 6$).

Variation of the stroke with the normalized channel radius is shown in Figure 3.3c for a fixed wavelength, $\lambda/s = 3$, and the normalized tail length, L/s, values varying between 2 and 8. As the channel radius increases, the stroke increases rapidly between

$R_{ch}/r = 1.25$ and $R_{ch}/r = 3$, then continues to increase slowly up to $R_{ch}/r = 6$, and does not vary significantly for larger values of R_{ch}/r; in effect, the free-swimming conditions apply for $R_{ch}/r > 6$.

For constant tail length, $L/s = 6$, the variation of the stroke with respect to channel radius is shown in Figure 3.3d, for normalized wavelengths, λ/s, varying between 1 and 6. For $\lambda/s = 1$ and 6, as the channel radius increases, the stroke increases rapidly first than decreases slightly. However, for normalized wavelength values equal to 2, 3 and 4, the stroke does not go through a maximum. Moreover, the stroke is the largest for $\lambda/s = 3$ for all values of the normalized channel radius.

Decreasing swimming velocity in narrow channels is due to increasing drag force on the body, which is analytically calculated for some objects. For example Happel and Brenner [49] show that channel restriction causes increased drag on the sphere which moves axially through a cylindrical tube. As the normalized channel radius approaches to one, the cell plugs the channel and the displaced fluid in front of the cell cannot flow over the body and results in infinite drag, and zero swimming velocity. These results are consistent with previous studies on artificial microswimmers; Temel and Yesilyurt [30] showed that displaced fluid in front of the swimmer flows over the body and contributes to increased drag. Furthermore, in our previous work on artificial structures with cylindrical bodies swimming in cylindrical channels, as the radius of the body increases, the increasing drag force on the swimmer leads to reduced forward velocity of the swimmer [50].

Moreover, the propulsion force is expected to increase near solid boundaries and result in an increase in swimming velocities as reported in [31] for swimming between parallel plates, and as observed for $\lambda/s = 1$ in Figure 3.3d. The trade-off between the drag on the spheroid body and the flagellar propulsion force leads to small variations in the swimming velocity unless the cell is very close to the wall; however in some cases, especially for tails with large radii, flagellar force is dominant as discussed below and reported in [34].

3.2   Power Efficiency

Power efficiency of swimming, which is given by Eq. (1.15), is calculated as a function of the wavelength and the tail length for wide ($R_{ch}/r = 13.5$) and narrow (R_{ch}/r

= 3) channels. For the wide channel, maximum swimming efficiency is about 1.27% (Figure 3.4a), whereas it is 2.26% for the narrow channel (Figure 3.4b). For the wide channel, optimum normalized wavelength is three, $\lambda/s = 3$, and the normalized length of the tail is eight, $L/s = 4$. On the other hand for the narrow channel, the optimal wavelength is four, optimal normalized tail length is eight, $L/s = 8$. In the narrow channel (Figure 3.4a), the power efficiency increases monotonically with the normalized tail length up to $L/s = 8$ for all λ/s.
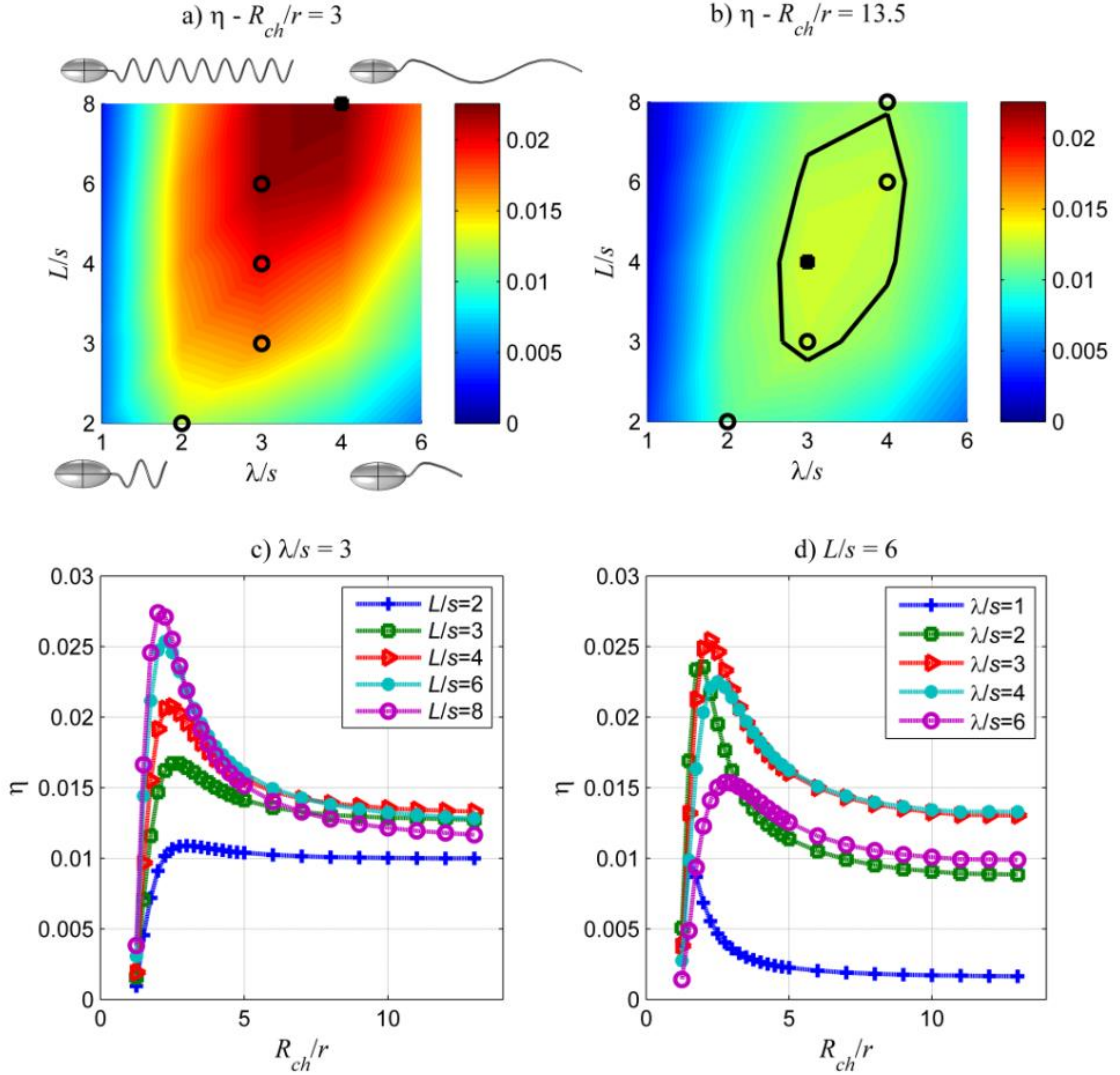
Figure 3.4 Surface plots of the power efficiency of swimming, η, as a function of the normalized wavelength and the normalized tail length for (a) $R_{ch}/r = 3$, and (b) $R_{ch}/r = 13.5$. Black circles are the loci of maximum values for normalized tail lengths equal to 2, 3, 4, 6, and 8. Solid squares are the locations of the global maxima. Efficiency plots as function of the normalized channel radius for (c) a fixed wavelength, $\lambda/s = 3$, and (d) for fixed tail length $L/s = 3$.

However for the wide channel (Figure 3.4b) the power efficiency decreases with the tail length for $\lambda/s = 1$, 2 and 6, but goes through a maximum for $\lambda/s = 3$ and 4. For the wide

channel, there is an optimal region, where the efficiency is about 1.27% for $3 < \lambda/s < 4$ and $3 < L/s < 8$. Shapes of organisms for the four extremes of wavelength and tail length pairs are also shown in Figure 3.4a.

Even though the swimming velocity does not vary significantly for narrow and wide channels, the efficiency is significantly higher in the narrow channel with $R_{ch}/r = 3$ than the wide channel with $R_{ch}/r = 13.5$. The drag force on the body, which is the same as the propulsion force from the tail, is also higher in the narrow channel than the one in the wide channel. The viscous torque on the body is expected to be higher inside the narrow channel as well. However, the efficiency increase inside the narrow channel indicates that the increase in the torque is not as high as the one in the propulsion force which overcomes the drag. According to [49] the drag force on the sphere with the equal volume as the spheroid body of the cell is 2.32 times and the viscous torque is 1.10 times larger in the narrow channel than the wide channel confirming the two-fold increase in the efficiency.

The variation of the power efficiency with the channel radius is shown for the fixed wavelength in Figure 3.4c, and for the fixed tail length in Figure 3.4d. There is a critical radius of the channel, which varies between $2r$ and $3r$, for each geometry of the tail that the power efficiency reaches the maximum. For channels with radii smaller than the critical radius, the efficiency declines rapidly and goes to zero as the channel radius approaches to the radius of the body. For channels with radii larger than the critical radius, the efficiency declines rapidly first, but then levels out and converges to a limit for the free swimmer in the bulk fluid. Furthermore the maximum efficiency is larger for longer tails than shorter ones studied here, although there is an optimal tail length for the cell swimming in the bulk fluid.

In [4], authors report that the efficiency is very close to its maximum for a wide range of wavelength and tail length values as observed here. Moreover, optimal range of values does not change substantially for near wall and in free swimming conditions [4]. Here, it is observed that the efficiency in narrow channels can reach a value two times higher than the one in wide channels.

In Figure 3.5, the drag force on the body, which is the same as the propulsion force, is plotted against the normalized channel radius: for $\lambda/s = 3$ and varying tail lengths in Figure 3.5a; and for $L/s = 6$ and varying wavelengths in Figure 3.5b. In all cases, drag on the body increases with decreasing channel radius. Dependence of the body drag on

25

the tail geometry is due to the effect of hydrodynamic interactions between the body and the tail [51] and increases with the tail length.

In Figure 3.6, the flagellar torque is plotted with respect to normalized channel radius for $\lambda/s = 3$ and varying tail lengths (Figure 3.6a) and for $L/s = 6$ and varying wavelengths (Figure 3.6b). The flagellar torque increases with the tail length and decreases with the wavelength, or increases with the number of waves on the tail.
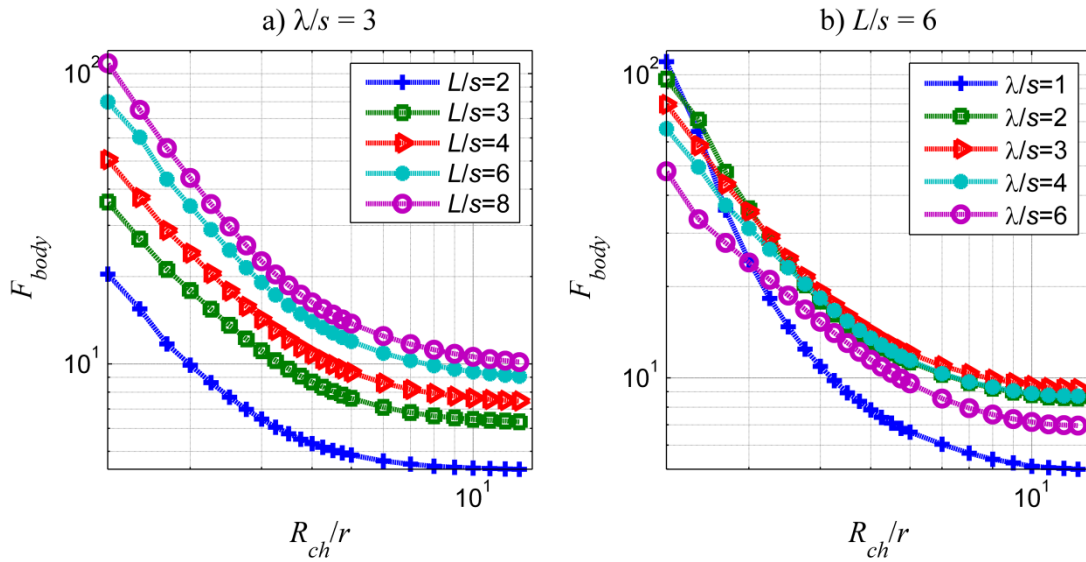
Figure 3.5 Drag force on the spheroid head, F_{body} [fN], as a function of the normalized channel radius for (a) the fixed wavelength, $\lambda/s = 3$, and (b) tail length, $L/s = 6$.
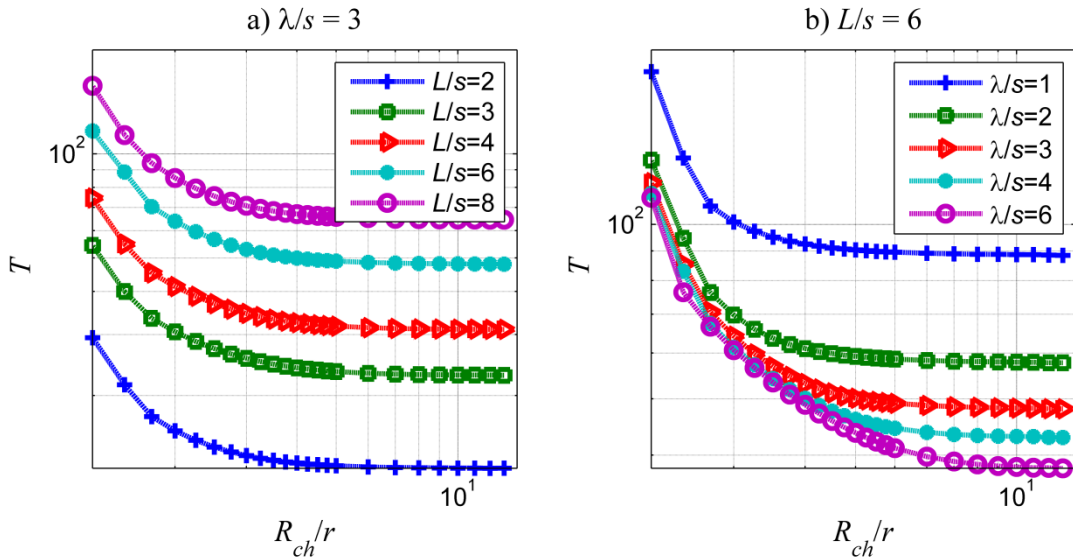
Figure 3.6 Flagellar torque, T [pN-nm], as a function of the normalized channel radius for (a) the fixed wavelength, $\lambda/s = 3$, and (b) tail length, $L/s = 6$.

3.3 Lateral Velocities

As reported in literature, e.g. [19, 52], bacteria follow helical trajectories during swimming. The radius of the helical trajectory is determined by the magnitude of lateral velocities in perpendicular directions to the forward motion. In this study, we computed the velocities of the cell in lateral directions, (**y**- and **z**- directions in Figure 2.6), for angular rotations of the tail between $\pi/6$ and 2π by $\pi/6$ intervals. It is observed that there is a $\pi/2$ phase angle between the velocities in **y**- and **z**- directions (not shown here), which have the same magnitudes, indicating that the cell, in effect, follows a helical trajectory.
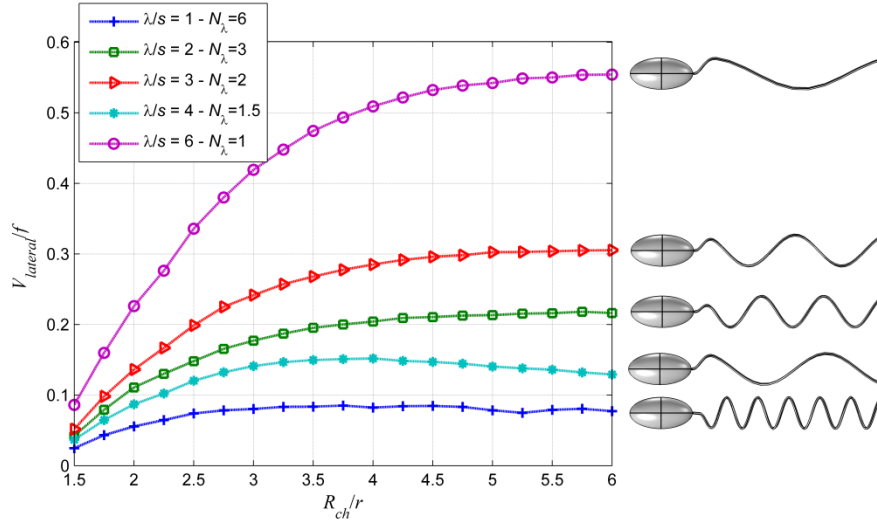
Figure 3.7 Magnitude of the lateral stroke, $V_{lateral}/f$ [μm], is plotted as a function of the normalized channel radius, R_{ch}/r, for different wavelengths and a fixed tail length, $L/s = 6$.

In Figure 3.7, the effect of the channel radius on the magnitude of the lateral stroke, which is defined as, $V_{lateral}/f = \sqrt{V_{sw}^2 + W_{sw}^2}/f$ here, is shown for a fixed tail length, $L/s = 6$, and for varying values of wavelengths between $\lambda/s = 1$ and 6. The lateral stroke increases sharply for the values of the normalized channel radius between 1.5 and 4 and then increases slightly between 4 and 6; further increase in the channel radius does not lead to significant change in the lateral stroke (not shown here). For normalized values of $\lambda/s = 1$, 2, 3 and 6, as the wavelength increases the lateral stroke increases. For $\lambda/s = 4$, the magnitude of the lateral stroke is larger than the one for $\lambda/s = 1$ but smaller than the one for $\lambda/s = 2$. The envelop region that defines the smooth increase of the helical radius near the body of the cell contributes to the imbalance in the rotation of the helices

with integer number of turns. Shapes of organisms are also shown in Figure 3.7 to improve the visualization of the effects of the helical shape.

In order to demonstrate the effect of the number of turns as an important parameter that governs the lateral stroke, we performed simulations for fixed tail length, $L/s = 6$ and channel radius, $R_{ch}/r = 4$, by varying the number of helical turns, N_λ. In Figure 3.8, the effect of N_λ on the magnitude of the lateral stroke, $V_{lateral}/f$, is presented. In general, the lateral stroke decreases with the number of helical turns, and goes through peaks and troughs depending on the number of helical turns. Typically peaks are observed at half integers and troughs at full integers in literature [53]. The contribution from the envelop region that breaks the symmetry near the joint, thus the lateral stroke achieves local maxima for $N_\lambda = 1, 2, 3, 4.25$, and minima for $N_\lambda = 1.5, 2.5, 3.75$.
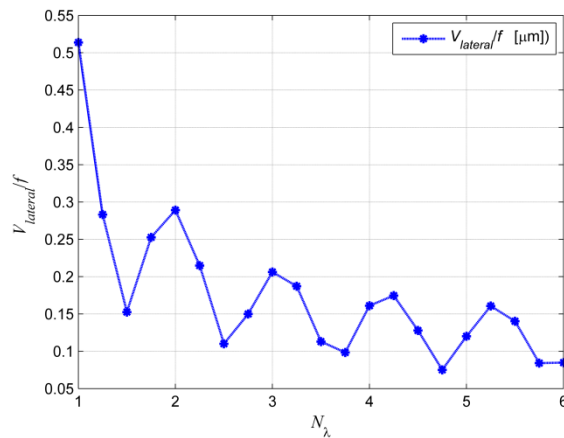
Figure 3.8 Magnitude of the lateral stroke, Vlateral/f [μm], as a function of Nλ for fixed channel radius, Rch/r = 4, and tail length, L/s = 6.

Effects of solid walls on the motion of microorganisms are well-reported in literature; and observations agree with the results presented here. In particular, there are several studies report that the lateral motion due to Brownian or hydrodynamic effects are suppressed near solid boundaries [32, 37, 4, 27, 54]. Berg and Turner [16] report that the bacteria align with the axis of the channel and the lateral motion is suppressed significantly inside channels. Moreover, Liu and Papadopoulos [17] report that that randomness in the locomotion of bacteria is reduced in capillaries compared to the locomotion in the bulk. Our results indicate that lateral motion is also suppressed in narrow channels similarly to the suppression of Brownian motion in capillaries.

3.4   Wobbling Rate

Angular velocities in lateral directions, Ω_y and Ω_z, indicate the wobbling rate of the bacterium. In Figure 3.9, the magnitude of the wobbling rate, $\Omega_{wobbling} = \sqrt{\Omega_y^2 + \Omega_z^2}$ is plotted with respect to normalized channel radius, R_{ch}/r, and for normalized values of the tail length, L/s, between 2 and 8 and for a fixed wavelength, $\lambda/s = 3$. In all cases, the magnitude of lateral angular velocities is much smaller than the rotation rate of the tail in the axial direction; for $L/s = 2$, the maximum is about 0.075 for the unit rotation rate of the tail. Magnitude of the wobbling rate decreases as the channel radius decreases, similarly to the effect observed in lateral velocities. It is reported in literature that natural organisms tend to align with the axial direction of the channel as the channel radius decreases consistently with the reduced lateral velocity as well as the wobbling [16].
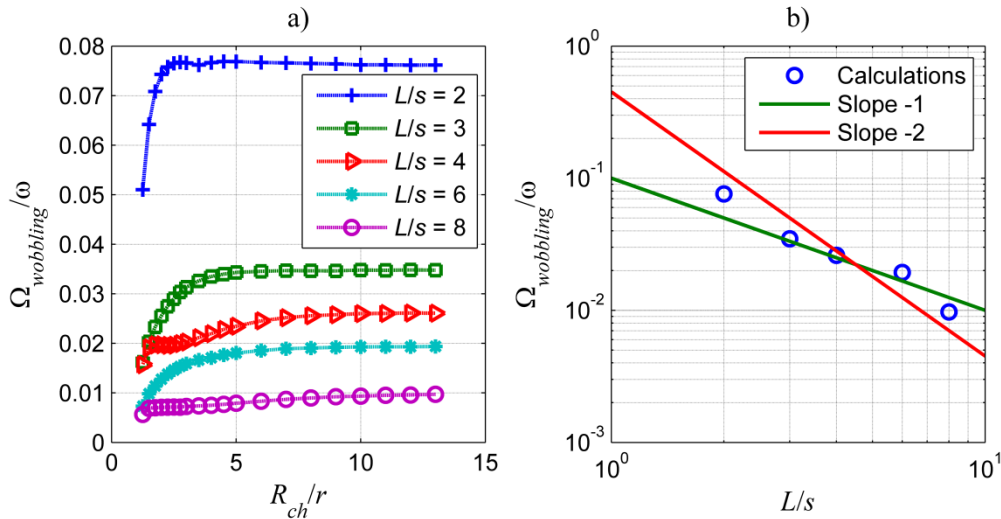
Figure 3.9 (a) Wobbling rate of the bacterium with respect to the normalized radius of the channel, R_{ch}/r, for $\lambda/s = 3$ and $L/s = 2$ (blue plus signs), 3 (green squares), 4 (red left-triangles), 6 (cyan stars) and 8 (magenta circles). (b) Relationship between wobbling rate and tail length for wide channels ($R_{ch}/r = 13$), blue circles represent the wobbling rates.

Furthermore, as the tail length increases wobbling rate decreases due to increasing resistance to lateral rotations; it is harder to rotate an organism with a longer tail than a shorter one. In fact, the wobbling rate is the highest in the case of the shortest tail, $L/s = 2$. For $L/s = 2$, 3 and 6, wobbling rate increases sharply for $1.5 < R_{ch}/r < 3$, and slowly for $R_{ch}/r > 3$. For $L/s = 4$, and mildly for $L/s = 8$, there is a slight increase in the

wobbling rate for $4 < R_{ch}/r < 6$, due to hydrodynamic interactions between the tail and the channel wall (see Figure 3.9a).

Wobbling behavior of the bacteria is also observed during the motion of artificial helical flagella, which are actuated with external magnetic fields [54]. Man and Lauga [55] discussed that the visible angle of wobbling is proportional to the wobbling rate for a fixed geometry of the helix and varies inversely with the dimensionless Mason number, Ma, which is defined as the ratio of viscous torques to magnetic torques. At high values of Ma the swimmer achieves directional propulsion, whereas at low values wobbling prevails [37]. In case of microorganisms with helical tails the magnetic torque is replaced by the motor torque and the effective viscous torque increases as the channel diameter decreases, and stabilizes the wobbling (see Figure 3.2b and Figure 3.9a). Moreover, for large channels the Ma is smaller and according to [37], the wobbling rate varies inversely with the square of the tail length (see Figure 3.9b).

3.5 Effect of Tail Radius (R_{tail})

Combined effects of the radius and the length of the tail and the channel radius are studied here, while the normalized wavelength is fixed, $\lambda/s = 3$. The normalized radius of the tail, R_{tail}/r, is varied between 0.063, which is the base case, and 0.315; the base case corresponds to $0.05a$, where a is the radius of the sphere which has the same volume as the spheroid head as adopted in [4]. The stroke increases with the radius of the channel for the base value of the tail radius in Figure 3.10a. However as the radius of the tail increases it is observed that the stroke goes through maximum at a critical channel radius. The presence of the maximum stroke is distinguishable for $L/s = 8$ for $R_{tail}/r = 0.126$ in Figure 3.10b, and as the tail radius increases further, the maximum stroke is observed for shorter tails as well. In Figure 3.10e, the stroke reaches the maximum for all tails studied here.

For $L/s = 2$, the stroke increases with the tail radius for any channel radius in Figure 3.11a. However for $L/s = 8$ in Figure 3.11e, there is a crossover: the stroke increases with the tail radius in narrow channels for $R_{ch}/r < 4$, and changes the trend in wide channels.
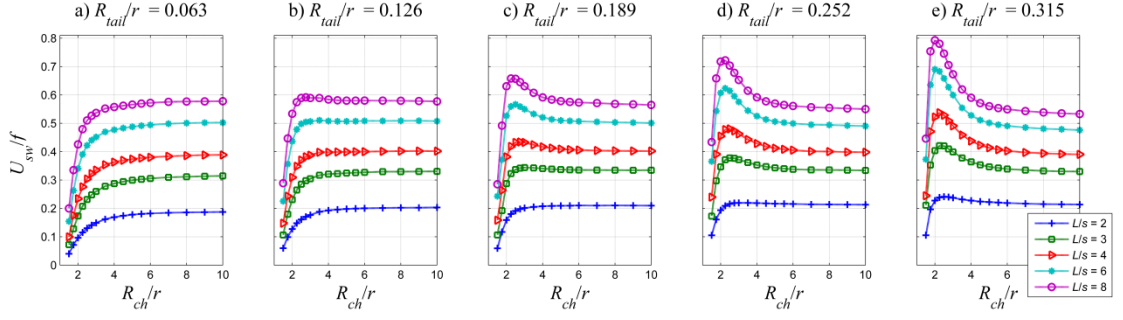
Figure 3.10 The stroke, U_{sw}/f [μm], as a function of the normalized channel radius, Rch/r, and the normalized tail length, L/s, and for (a) $R_{tail}/r = 0.063$; (b) $R_{tail}/r = 0.126$; (c) $R_{tail}/r = 0.189$; (d) $R_{tail}/r = 0.252$; and (e) $R_{tail}/r = 0.315$.

Normalized values of the critical radius of the channel, for which the stroke is maximum, are listed in

Table 3.1   Critical Channel Radii

Table 3.1; values of the critical radius vary between $2 \leq R_{ch}/r \leq 3$. For a given tail length, critical radius of the channel decreases as the radius of the tail increases, but the critical radius is not observed for thinner tails as the length of the tail increases.
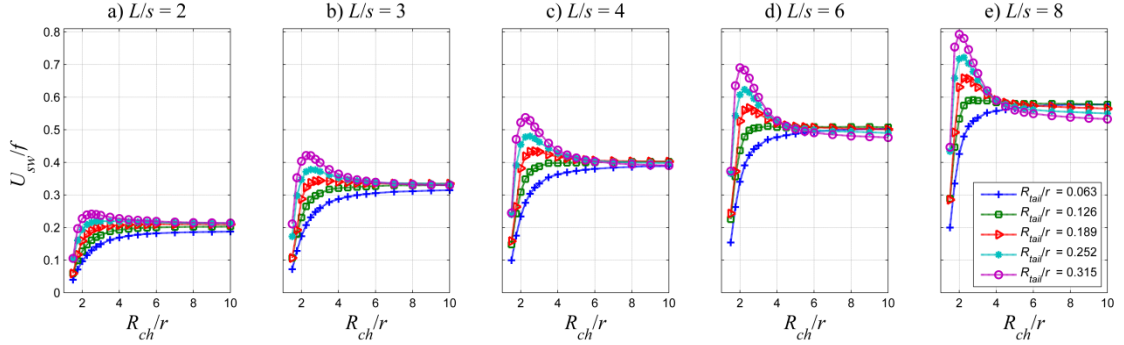
Figure 3.11 The stroke, Usw/f [μm], as a function of the normalized channel radius, R_{ch}/r, for the normalized tail radius, R_{tail}/r, values varying between 0.063 and 0.315, and for (a) $L/s = 2$; (b) $L/s = 3$; (c) $L/s = 4$; (d) $L/s = 6$; and (e) $L/s = 8$.

The power efficiency of the bacteria swimming in circular channels is revisited for R_{tail}/r values varying between 0.063 and 0.315 and for L/s between 2 and 8 in Figure 3.12. The efficiency increases with the tail radius in narrow channels, but decreases in wide channels. For $L/s = 6$ the maximum efficiency is observed as 0.0327 for $R_{tail}/r = 0.126$, which is considerably higher than 0.0132 for $R_{tail}/r = 0.063$ (Figure 3.12e). There is an optimal channel radius, which provides the maximum swimming efficiency. As the tail radius increases, optimal channel radius decreases; for $R_{tail}/r = 0.315$, the

optimal channel radius is about $R_{ch}/r = 1.75$, whereas for $R_{tail}/r = 0.063$, the optimal channel radius is $R_{ch}/r = 2.25$.

Table 3.1   Critical Channel Radii

Critical R_{ch}/r						
		R_{tail}/r				
		0.063	0.126	0.189	0.252	0.315
L/s	2	-	-	-	3	2.5
	3	-	-	3	2.5	2.25
	4	-	-	2.75	2.5	2.25
	6	-	3	2.5	2.25	2
	8	-	2.75	2.25	2.25	2

The crossover in the efficiency takes place for $R_{ch}/r \approx 3$ for all tails. Increase in the efficiency of helical swimming in circular channels is also discussed in [34] based on analytical results obtained from the perturbation theory for infinite helices in channels. Furthermore, inside the channel with $R_{ch}/r = 10$ and for $L/s = 8$, the efficiency for the tail with the smallest radius is 0.0122 and for the one with the largest is 0.0035.
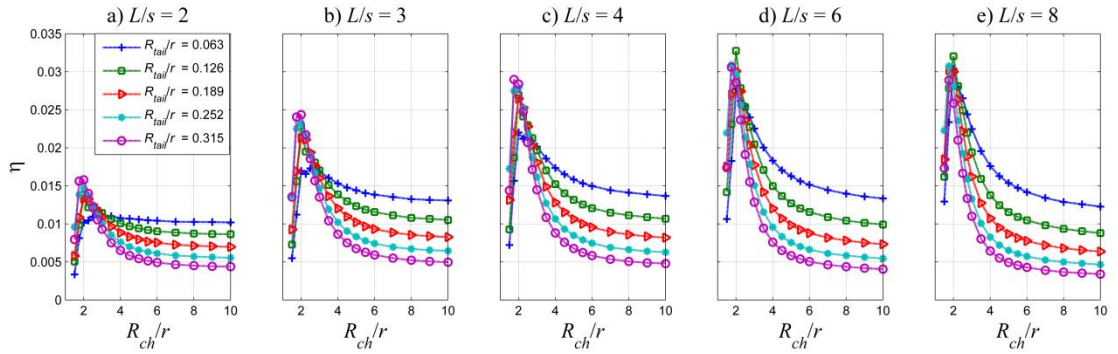
Figure 3.12 The efficiency as a function of the normalized channel radius, R_{ch}/r, for the normalized tail radius, R_{tail}/r, values varying between 0.063 and 0.315, and for (a) $L/s = 2$; (b) $L/s = 3$; (c) $L/s = 4$; (d) $L/s = 6$; and (e) $L/s = 8$.

4   EFFECTS OF GEOMETRIC PARAMETERS ON THE SWIMMING OF ARTIFICIAL SWIMMERS

4.1   Experiments

According to the experiments, swimmers exhibit distinct swimming modes with respect to the frequency of the rotating magnetic field. At low frequencies (1 - 5 Hz), the swimmer motion takes place very close to the wall due to gravity. In the transition period (5 - 20 Hz), the lift force due to the rotating flow in the channel becomes sufficiently large and leads to swimming away from the wall in the core region of the channel. The swimmer reaches its maximum velocity in the axial direction (in the **x**-direction) along the channel in the transition period. At very high frequencies, the swimmer loses synchronization with the magnetic field and cannot sustain a continuous motion, since the magnetic torque cannot overcome the viscous drag torque.
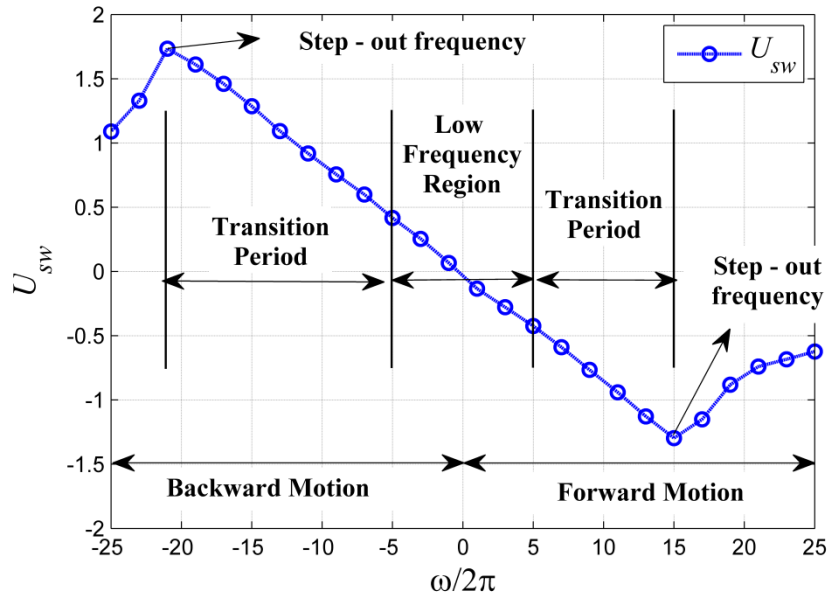
Figure 4.1 The swimming modes of swimmers with respect to frequency. (U_{sw} [mm/s]; $\omega/2\pi$ [1/s])

The limit "step-out" frequency can vary with the geometric parameters of the helical tail, amplitude of the magnetic field, and flow conditions. After the step-out frequency, the motion of the swimmer is irregular. The swimmer moves arbitrarily in the all directions with a decreasing velocity (Figure 4.1).

4.1.1 Channel Effect

We performed experiments to elucidate the effect of the channel diameter on the velocity of the swimmer for three robots with difference dimensions in wide channel (D_{ch} = 2.5) and narrow one (D_{ch} = 1.6).

Table 4.1   Dimensions of Robots P1, P2 and P3. D_{head} is diameter of the head, λ is wavelength, L is the total length of the swimmer.

Robots	D_{head} [mm]	λ [mm]	L [mm]	N_λ
P1	1	0.5	3	3
P2	1	0.5	2.5	2
P3	1	0.5	2.5	2

Dimensions of the robots P1, P2 and P3 are represented in Table 4.1. Based on the numerical studies in our previous study [40], it is known that as length of the helical tail is increased, swimmer velocity increases. Due to close dimensions, velocities have similar values (Figure 4.2). In the wide channel, forward and backward velocity profiles follow the same trend for three robots. The step-out frequency for forward motion is considerably higher in the wide channel than the one in the narrow channel. Hydrodynamic flagellar torque is increasing rapidly as the channel diameter (D_{ch}) approaches to the diameter of the swimmer head (D_{head}) (Acemoglu and Yesilyurt, 2014). In narrow channels, as frequency increased, the synchronization of the hydrodynamic and magnetic torques is lost at lower frequencies (~10 – 15 Hz) due to the increase in hydrodynamic force; however in wide channels step-out frequency is ~20 – 25 Hz. Moreover, the swimmers start to follow a helical trajectory at 5 Hz. As frequency is increased, the radius of the helical trajectory increases and the swimmer hits the channel wall frequently with an irregular motion. It is suspected that the magnetic torque on the swimmer may contribute to the instability as the orientation of the swimmer is not aligned with the long axis of the channel, which is the same as the direction of the rotating magnetic field. As the frequency is increased further, increasing

contact of the swimmers with the wall hinders the forward motion. However the swimmers can propel at higher frequencies in the wide channel since the swimmer wall - interactions are not as much effective as the ones in the narrow channel.

For backward motion, higher backward velocities are observed in the narrow channel due to the restriction. Decreasing the channel diameter causes an increase in the swimmer velocity up to a critical channel diameter [40]. In these experiments, for backward motion, we observed that backward motion is faster in the narrow channel (Figure 4.2). There are two main reasons to observe higher velocities in the narrow channel. Firstly, when channel diameter is decreased, traction force starts to become dominant and contributes to the velocity of the swimmer. Secondly, the swimmer follows a straight trajectory close to the long axis of the channel in the backward motion, which means energy loss due to swimmer - wall interactions is less than the one in the forward motion. For only P2 backward velocity in the narrow channel is very close to backward velocity in the wide channel. Moreover, in the backward motion, the swimmer can reach higher frequencies than the step-out frequency in the forward motion, since it follows a straight trajectory in the both narrow and wide channels. Because the stability of the helical trajectory in the forward motion is less than the straight trajectory in the backward motion; as frequency increases, synchronization with magnetic field is lost at lower frequencies in the forward motion.
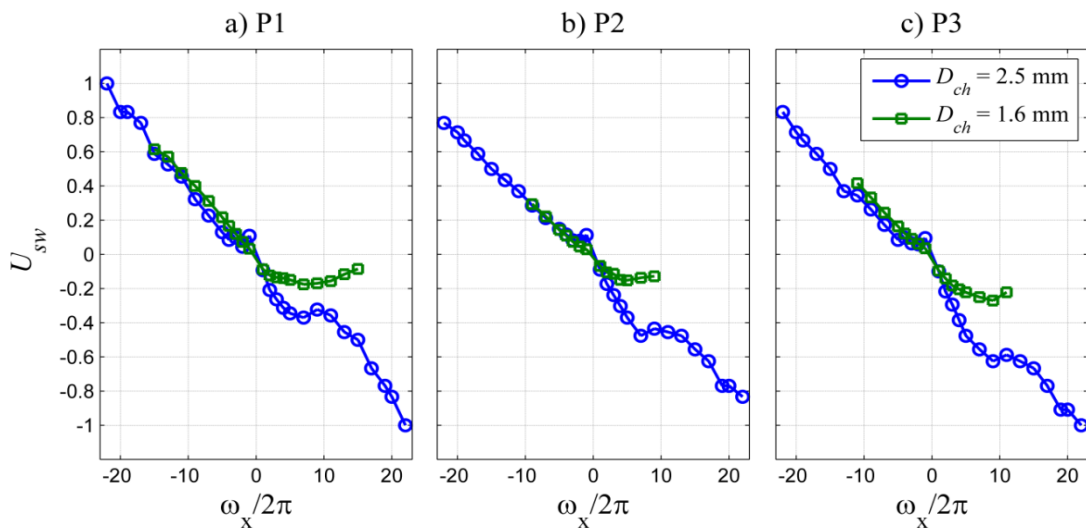
Figure 4.2 Swimming velocities, U_{sw} [mm/s], for Robots P1, P2 and P3 in wide and narrow channels.
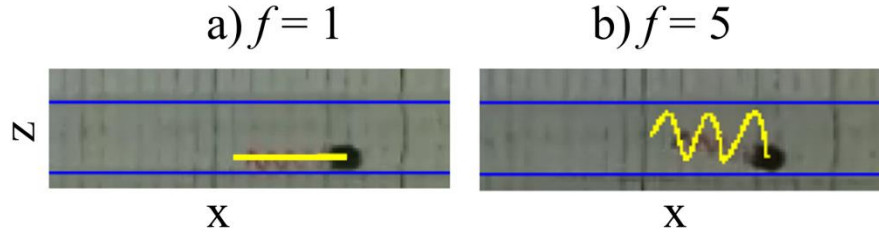
Figure 4.3   Positions and trajectories (yellow lines) of the swimmer at low (f = 1 Hz) (a) and high (f = 5 Hz) (b) frequencies. Channel walls are highlighted with blue lines. The swimmer propels at the bottom of the channel at low frequencies (a) and near channel center at high frequencies (b).

In order to determine the position of swimmer in the channel, we compare our experiment results with simulation results. Simulations are performed by placing the swimmer in the channel center and near channel wall. In experiments, the swimmer propels the near wall at low frequencies due to weight of the swimmer (Figure 4.3a). At transition frequencies, the swimmer takes lift force and starts to swim close to the channel center (Figure 4.3b). Our simulation results demonstrate that at low frequencies, the experiment results agree well with the near-wall simulation results (Figure 4.5c-d); whereas at transition frequencies they agree with simulations in the channel center (Figure 4.5a-b). Thus, experimental observations are validated with our CFD model. Both in wide and narrow channels, backward velocities agree well with the center simulations; whereas forward velocities does not follow same trend with the simulation results due to non-stable helical motion.
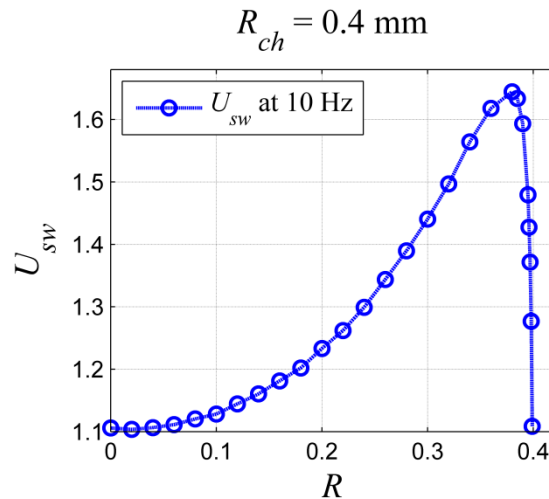
Figure 4.4   Radial position, R [mm], effect on swimming velocity U_{sw} [mm/s], (at center $R_{ch} = 0$).

Beside these results, there is an optimum radial position that maximizes the forward velocity. As the swimmer approaches the channel wall, forward velocity increases; if it is very near the channel wall, velocity decreases rapidly due to friction (Figure 4.4).
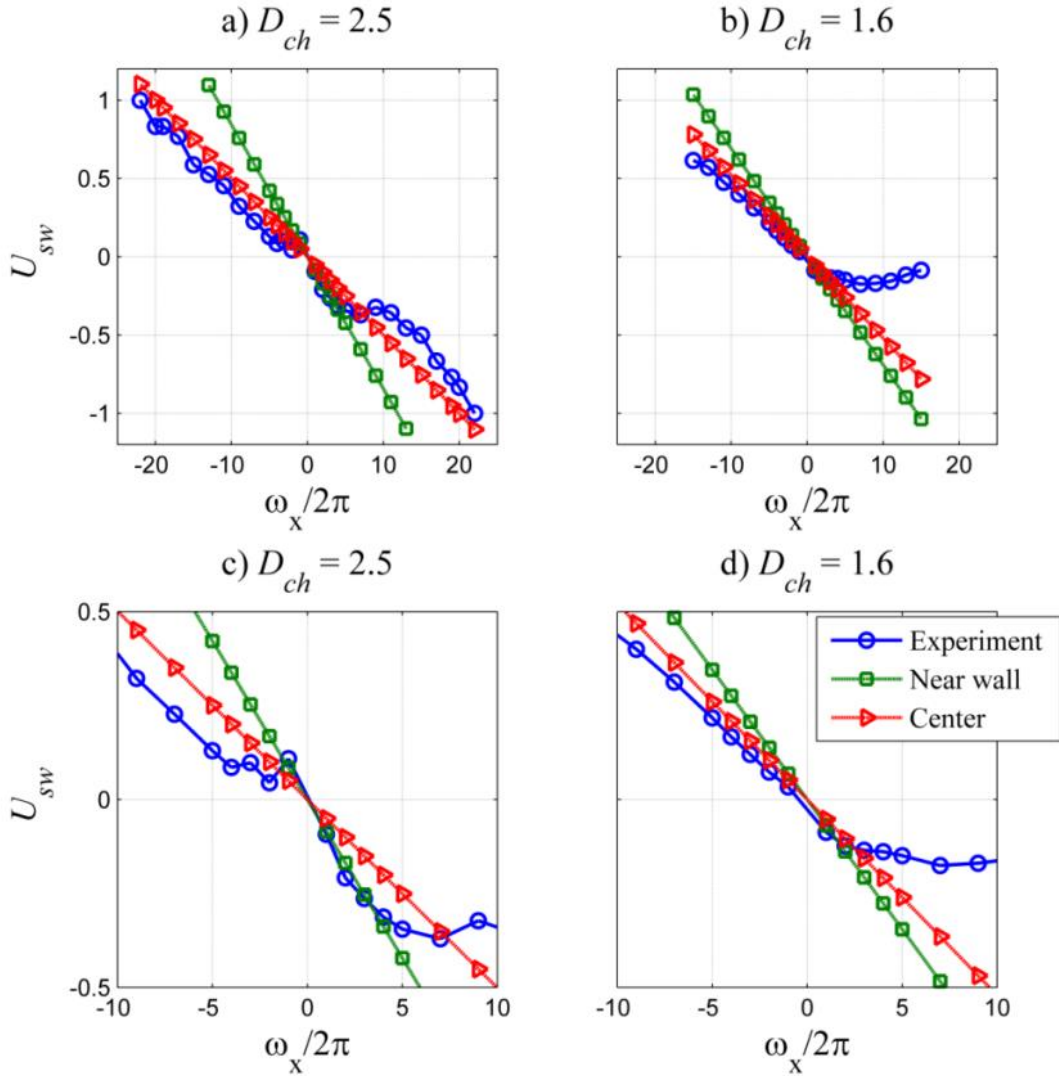
Figure 4.5 Comparison of experimental results with simulation results for Robot P1. (*blue circles* are experimental results, *green squares* are near wall simulation results, *red triangles* are the channel center simulation results). a) D_{ch} = 2.5 mm, b) D_{ch} = 1.6 mm, close-up for low frequencies, c) D_{ch} = 2.5 mm, d) D_{ch} = 1.6 mm.

4.1.2 Wavelength Effect (constant tail length (L))

Three different robots are manufactured with different wavelengths and fixed tail length. Experiments are performed in the circular channel with a diameter 1.6 mm. The tail length (L) of the robots is 1.8 mm and the wavelengths (λ) are 0.4, 0.6 and 0.8 mm for Robot S1, S2 and S3, respectively (Figure 4.6) Swimming velocity results are

demonstrated in Figure 4.7. Robot S2 can reach higher swimming velocities at high frequencies than Robot S1 and S3; in literature it is also reported that for fixed tail length, there is an optimum N_λ which maximizes swimming velocity [35, 38]. In Figure 4.7, Robots S2 and S3 whose (N_λ) are 2.25 and 3 perform faster motion than Robot S1 ($N_\lambda = 4.5$). Robot S1 has the lowest velocity; because of low thrust force provided by the tail. The tail geometry of the Robot S1 does not let the fluid enter the inside of the tail since the wavelength is short; during motion, the fluid passes over the tail with very limited interaction with the entrapped fluid inside the tail. Thus Robot S1 cannot displace the fluid as much as Robot S2 and S3 can. The channel center leads to reach high frequencies without step-out in the backward motion (Figure 4.7). Additionally, backward velocity can reach higher values (e.g. 1 mm/s), whereas maximum forward velocity is ~0.6 mm/s.

In Figure 4.7, velocities of Robot S2 and S3 are very close to each other; however their low and high frequency responses are slightly different. For forward motion, S3 is faster than S2 up to 10 Hz, S2 has slightly higher velocities after 10 Hz up to step-out frequency (Figure 4.7). For backward motion, the crossover is observed at about 12 Hz.
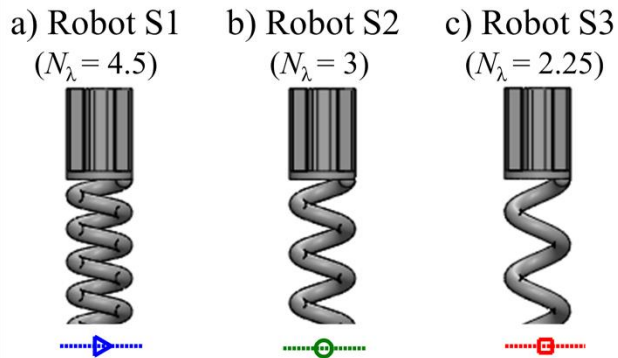
Figure 4.6   Tail geometries that are produced with different wavelengths where tail length is constant.

A comparison of the data obtained from the numerical studies and the experiments are depicted in Figure 4.8. For Robot S1, swimming velocities obtained from the experiments are lower than the simulation results (Figure 4.8a). During 3D printing process, support material is placed between the helical pitches; after printing process support material is removed from the body. Tail geometry is like a solid body with the effect of the remaining support material on helical tail. Because of this, ideal propulsion obtained from simulations does not match with the experimental data. The center simulation results for Robot S2 are very close to the experimental ones for backward

motion (Figure 4.8b), moreover experimental observations validate that backward motion is stable in the channel center not only for Robot S2 but also all other swimmers that used in the experiments. For forward motion of Robot S2, swimmer follows a helical trajectory around channel wall; near wall simulation results are consistent with experimental results. For Robot S3, experimental swimming velocities match with the velocities from the center simulations; whereas the experimental backward velocities are slightly lower than the simulations (Figure 4.8c).
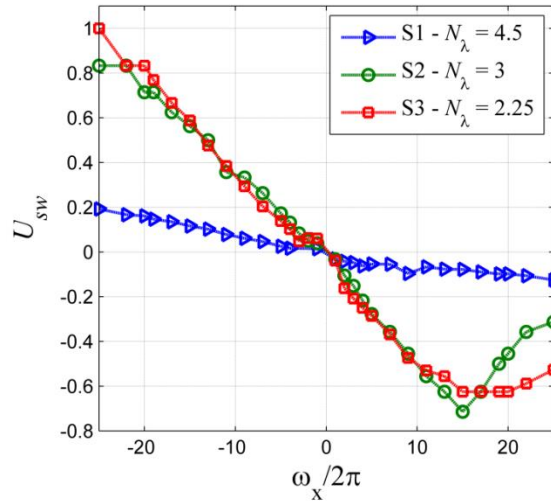
Figure 4.7 Wavelength effect on swimmer velocity, U_{sw} [mm/s], for Robots S1, S2 and S3 presented in Figure 4.6. Robot S1 - λ= 0.4 mm - N_λ = 4.5, *blue triangles*; Robot S2 - λ= 0.6 mm - N_λ = 3, *green circles*; Robot S3 - λ= 0.8 mm - N_λ = 2.25, *red squares*.
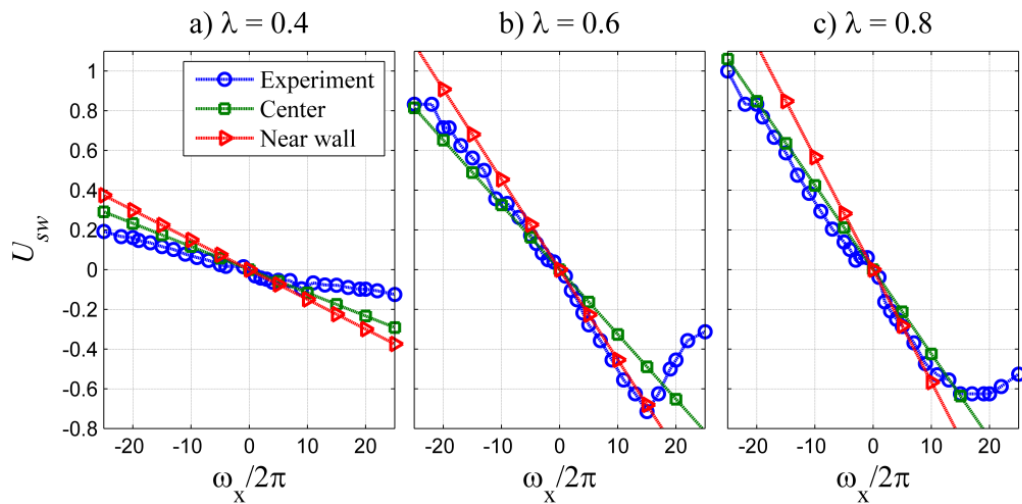
Figure 4.8 Swimming velocity, U_{sw} [mm/s], comparison of experimental and simulation results for wavelengths a) λ = 0.4 mm, b) λ = 0.6 mm, c) λ = 0.8 mm.

4.1.3 Effects of Number of Waves (constant wavelength, λ)

Robot R1, R2 and R3 have constant wavelength ($\lambda = 1$ mm) and 6, 4, 2 mm tail lengths respectively. In Figure 4.9, swimming velocities, U_{sw}, are represented for these three robots. As tail length is increased, forward and backward velocities increase due to greater thrust force applied by the tail. The fluid displaced by the tail increases as the total surface area of the tail is increased. Although it is known that there is an optimal tail length (L) which maximizes U_{sw} for fixed wavelength [40], experiment results demonstrate that U_{sw} increases with increasing tail length (Figure 4.9a). According to simulation results as tail length L is increased, U_{sw} increases up to $L = 8$ mm (Figure 4.9b). The optimum value of tail length is dependent with L_{tail}/R_{head} and R_{tail}/R_{head} as reported in [34]. Here our R_{tail}/R_{head} parameter is equal to 0.25. Felderhof [34] reports that R_{head}/R_{tail} must be equal to 0.02 to observe optimum tail length. Since our model has a thick tail, optimum tail length is not observed in both experimental and computational works.
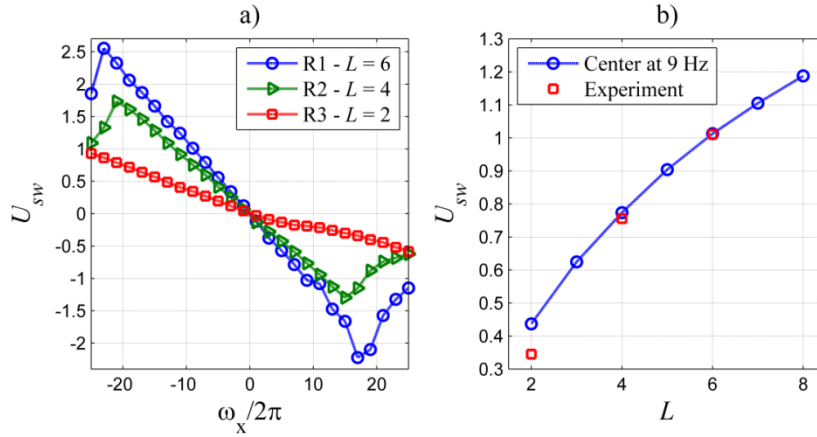
Figure 4.9 a) Tail length effect on swimming velocity, U_{sw} [mm/s], for Robots R1, R2 and R3 who have constant wavelength, $\lambda = 1$ mm, where channel diameter (D_{ch}) is 1.6 mm. b) Swimming velocity, U_{sw}, – tail length, L, simulation results in the channel center for 9 Hz; corresponding experimental values are shown with red squares.

Simulations for the same swimmer geometries as in the experiments also validate that experimental swimming velocities agree with center swimming velocities (Figure 4.10); observed swimming trajectories are in the center for backward motion and helical trajectories are around center line of the channel.
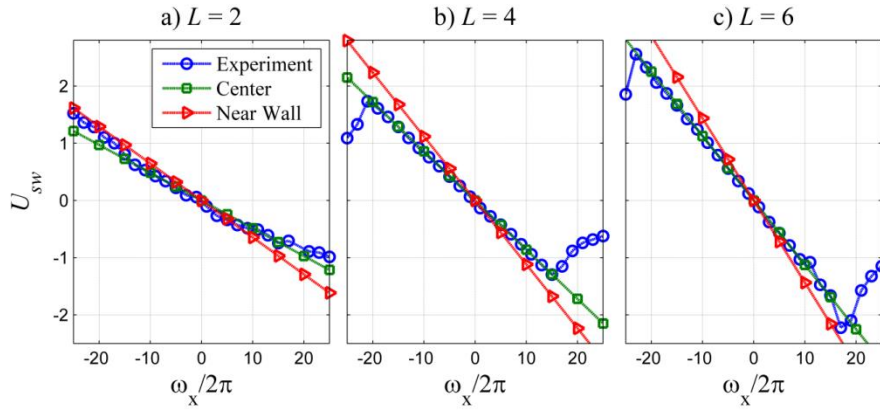
Figure 4.10 Experiment and simulation comparison for swimming velocities [U_{sw}, mm/s] of Robots R1, R2, and R3.

4.2   Simulations

Simulations are carried out to study effects of the radial position of swimmer, number of helical waves, wave amplitude (also the radius of the head) and the length of the cylindrical head. In the base case, swimmer has two helical waves with the length of the head equals to 600 μm, amplitude of the waves and the radius of the head equal to 200 μm, and is placed 20 μm away from the wall as shown in Figure 4.11a. In all simulations, the axis of the swimmer is kept parallel to the axis of the channel, which is 6 mm in length and 1 mm in diameter. In our experiments, we observe that the swimmer travels near the wall due to its weight and remains almost parallel to the axis of the channel.
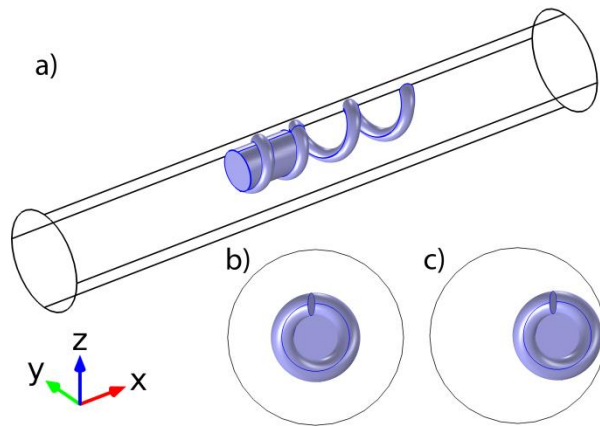
Figure 4.11 a) Isometric view of microswimmer in the channel; b) Back view swimmer in the center of the channel; c) Back view of the swimmer near the wall.

Simulations are performed using the non-dimensional values. In all simulations, angular velocity of the swimmer in the **x**-direction is set to a constant

41

value where frequency is 1 Hz, i.e. $\omega_x = 2\pi f$ for $f=1\ Hz$, $\omega_x=2\pi$.

4.2.1 Effect of the Radial Position

Radial position of the swimmer is varied in the **y**-direction for $z = 0$ (Figure 4.11b, c) while other parameters are kept constant. In total, ten different positions between the center and the boundary of the channel are used in simulations. The effect of the radial position on the velocity of the swimmer is shown in Figure 4.12a; velocities in the x, y and z-directions are plotted with respect to the distance between the channel wall and the swimmer, which varies between 20 and 110 µm for the base-case swimmer with two full waves on the tail and 200 µm amplitude. According to Figure 4.12a, magnitude of the forward velocity, U_{sw}, increases with decreasing distance between the channel wall and the swimmer. As the swimmer gets closer to the wall, traction forces are expected to increase and lead to increasing forward and lateral velocities. Minimum forward linear velocity is observed at the center of the channel as 0.088 mm/s (not shown in Figure 4.12a). According to our ongoing experiments, the robot with almost the same dimensions travels with 0.11 mm/s in a glass tube with the same dimensions as the channel; experimentally measured swimming velocity lies between the near-wall and in-center values obtained in simulations. It is difficult to obtain the radial position of the robot in the experiments, but due to its weight, robot travels closer to the wall than the center of the channel.
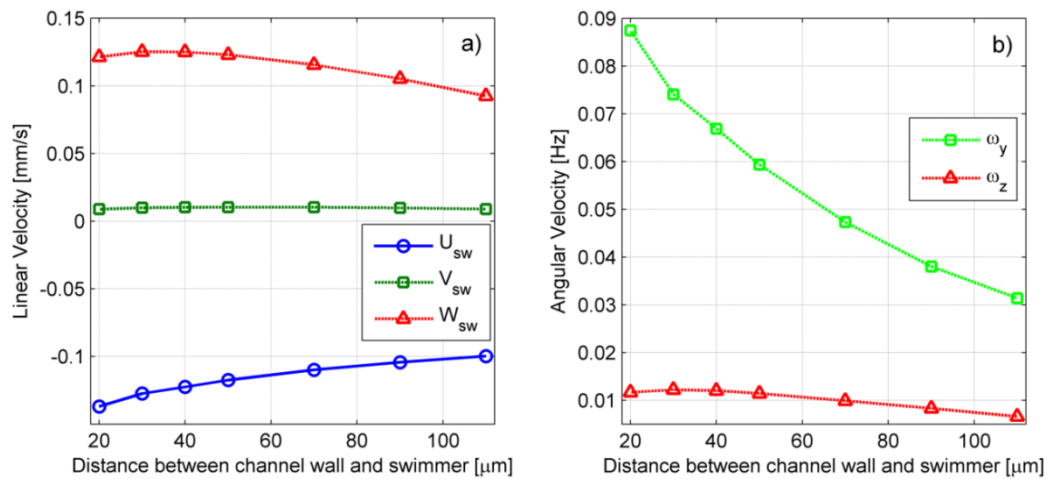
Figure 4.12 a) Linear velocity in the **x**-direction, U_{sw} (blue line with circles), in the **y**-direction, V_{sw} (green line with squares), and in the **z**-direction, W_{sw} (red line with triangles) vs. the distance between the wall and swimmer; b) Angular velocities about the **y** and **z**-axes vs. distance from the channel wall.

Magnitude of the **y**-direction velocity, V_{sw}, remains very small compared to velocity components in other directions and changes very slightly. The positive **y**-velocity indicates that the swimmer is pushed towards the wall with a decreasing trend as the swimmer becomes closer to the wall.

The velocity in the **z**-direction, W_{sw}, is always positive indicating that the swimmer tends to move with the flow induced by the rotation of the tail (see Figure 4.13). As the distance between the swimmer and the wall decreases, magnitude of the z-velocity increases. The maximum value of the **z**-velocity is observed when the distance from the wall is about 30 μm (Figure 4.12a). As the swimmer approaches further towards the wall, it is expected that the traction force between the swimmer and the wall will be dominant and the **z**-velocity will change its direction.
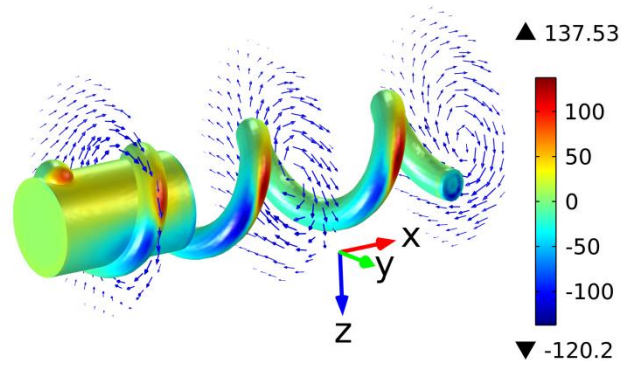
Figure 4.13   Velocity vectors (arrows) of the flow due to counter-clockwise rotation of the swimmer about the **x**-axis, and the pressure distribution (shaded colors) on the swimmer.

Angular velocities in **y** and **z**-directions are plotted against the distance from the wall in Figure 4.12b. Rotation of the swimmer about the **y**-axis corresponds to the yaw angle, which represents the heading of the robot with respect to the direction of its motion, and the rotation about the **z**-axis corresponds to the pitch angle, which represents the angle of attack with respect to the channel wall (see Figure 4.11). In simulations, the swimmer is perfectly aligned with the heading direction, i.e. yaw and pitch angles are set to zero, and angular velocities are calculated based on the torque-free swimming condition. A slight positive angular velocity in the **y**-direction, which is towards the wall here (see Figure 4.11), indicates that the swimmer is forced to turn to right (*head to starboard* in nautical terminology) with respect to its heading. Similarly, slightly positive angular velocity in the **z**-direction indicates that the swimmer tends to pitch up from the channel wall. As the swimmer approaches to the

wall, the yaw rotation rate increases due to increasing traction from the body; and the pitch rate first increases, goes through a maximum, then decreases as the swimmer approaches further towards the wall. The pitch rate of the swimmer follows the same trend as the **z**-velocity (see Figure 4.12a).

4.2.2 Effect of the Number of Helical Waves

Number of helical waves is varied between one and four for the base case swimmer with a fixed wavelength of 625 μm and positioned 20 μm away from the wall. In Figure 4.14a, linear velocity components of the swimmer are plotted against the number of helical waves on the tail. Magnitude of the forward velocity, U_{sw}, increases with increasing number of waves. However, the rate of increase tends to slow down as the number of waves increases. In literature, it is reported that there is an optimum number of helical waves that maximizes the forward velocity [30, 13].
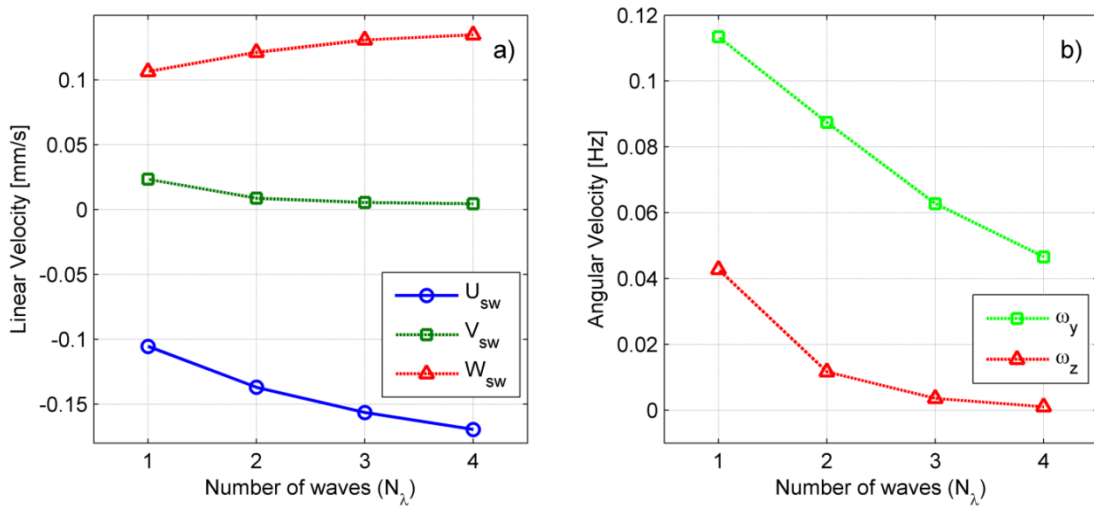
Figure 4.14   a) Linear velocities in **x**-, **y**- and **z**- directions vs. the number of waves for the swimmer placed near the wall; b) Angular velocities about the **y** and **z**-axes vs. the number of waves for the swimmer placed near the wall.

Radial velocity, which is in the **y**-direction here (see Figure 4.11), V_{sw}, decreases slightly with increasing number of waves, indicating that as the number of waves increases the swimmer's distance from the wall tends to remain stable. Swimmer's velocity in the **z**-direction, which is the tangential velocity with respect to channel coordinates, W_{sw}, increases with the increasing number of waves similarly to the forward velocity, U_{sw}. Since the **z**-velocity (tangential velocity according to

cylindrical coordinates) is influenced by the local rotating flow field around the swimmer, the increase in the **z**-velocity is due to the increase in the surface area of the swimmer with the number of waves.

As the number of waves increases, magnitudes of angular velocities about **y** and **z-**axes decrease as shown in Figure 4.14b. In principle, for a fixed wavelength as the number of helical turns increase, the length of the tail increases, and the distribution of periodic fluid forces over the tail becomes symmetric. Therefore yaw and pitch rotations of the swimmer about the center of mass diminish.

4.2.3 Effect of the Amplitude and Radius of the Head

For the swimmer with the base case dimensions and placed 20 µm away from the channel wall, the amplitude of helical waves, which is also the radius of the cylindrical head, is varied between 200 µm and 350 µm. Linear velocity components are plotted with respect to wave amplitude, B_0, in Figure 4.15. Forward velocity increases slowly with increasing wave amplitude up to the 300 µm, however, decreases sharply for 350 µm. It is well-established that the velocity of the swimmer increases with the amplitude of helical waves, e.g. [29, 31, 34, 38]. However, increasing the head size with the amplitude inside a channel increases the drag force on the head and reduces the velocity, and leads to decrease in the forward velocity.

Moreover, since the channel's inlet and the outlet are closed, displacement of the swimmer forces the fluid to displace backwards over swimmer and contributes to further increase in the drag. In Figure 4.16, the effect of increasing the diameter of the head along with the amplitude of helical waves is shown; the swimmer with a larger diameter of the cylindrical head covers larger portion of the cross section of the channel. Similarly to the forward velocity, velocities and **y** and **z**- directions also decrease sharply for B_0=350 µm.
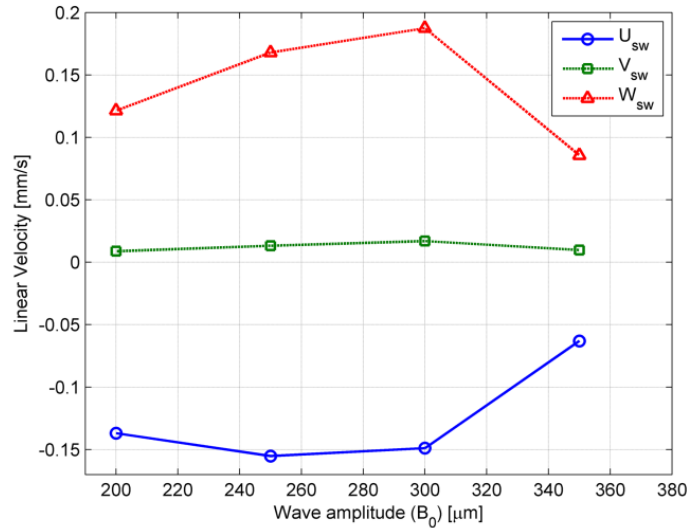
Figure 4.15　　　Linear velocities in **x**-, **y**- and **z**- directions vs. wave amplitude for the swimmer placed near the wall.
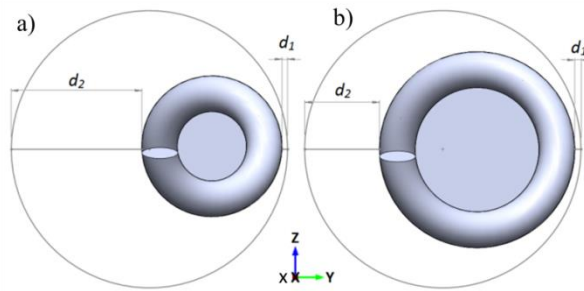
Figure 4.16　　　Distances between swimmer and channel wall, d_1 and d_2: a) For base case, $B_0 = 200$ μm; b) For $B_0 = 300$ μm.

4.2.4　Effect of the Length of Cylindrical Body

The length of the swimmer's body (head) is increased twice with respect to the base case swimmer (Figure 4.17a, b) and reduced by half (Figure 4.17c) to study the effect of the length of the body, while the total length of the helix including the portion which overlaps with the body is kept constant.

According to Figure 4.18, the magnitude of the forward velocity decreases with increasing length of the body owing to: first, decreasing length of the tail, which leads to less propulsion and slower forward velocity; and, second, increasing length of the body increases the drag force on the body. The velocity in the **y**- direction remains very small and decreases slightly due to decreasing effect of the tail since its relative length decreases as well. Lastly, the linear velocity in the **z**- direction increase with the body

length due to increasing surface area of the swimmer which is subject to a lateral drag due to rotating flow.
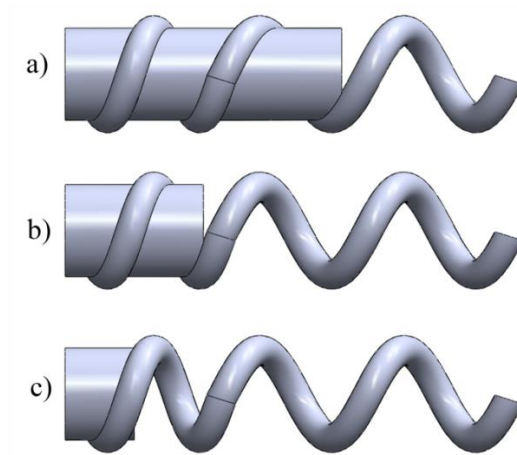
Figure 4.17   Swimmer with the body length twice as much as the one used in the base case; b) Base case swimmer; c) Swimmer with half head length of the base case swimmer.
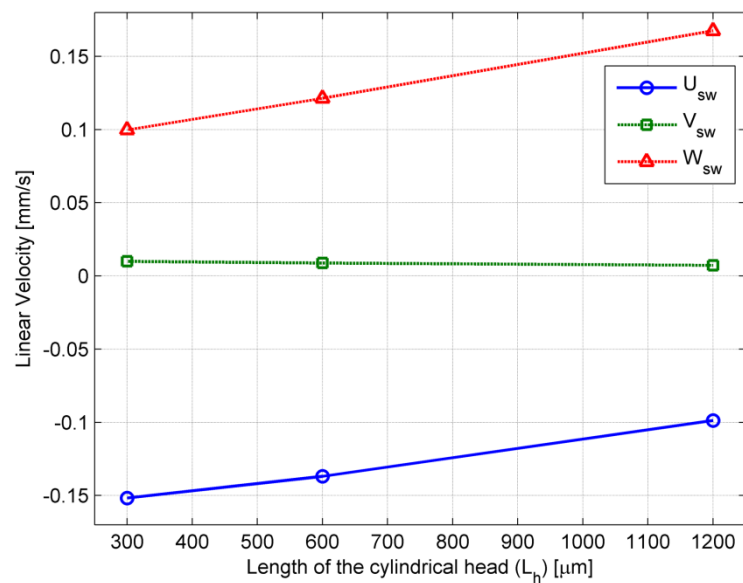
Figure 4.18   Linear velocities in **x**-, **y**- and **z**- directions vs. length of the body for the swimmer placed 20 μm away from the wall.

5   EFFECTS OF THE POISEUILLE FLOW IN THE CIRCULAR CHANNELS

The flow rate inside the channel with 1.6 mm diameter is varied between 0 and 75 µl/min by 25 µl/min intervals for the swimmers listed in Table 5.1. Robots R1, R2 and R3 have fixed length (L_{head}) and diameter of the head (D_{head}) and wavelength (λ). Number of waves is varied from 6 to 2 for Robots R1, R2 and R3. Reynolds Numbers for different flow rates are under unity ($Re << 1$) and presented in Table 5.2.
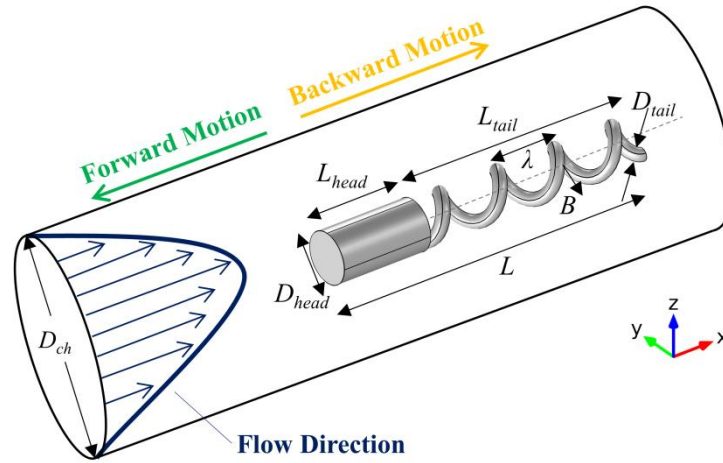
Figure 5.1 Schematic representation of the forward (head direction) and backward motion (tail direction) of the swimmer.

Table 5.1. Dimensions of Robots R1, R2, R3. D_{head} is diameter of the head, λ is wavelength, L is the total length of the swimmer.

Robots	D_{head} [mm]	λ [mm]	L [mm]	N_λ
R1	0.8	1	8	6
R2	0.8	1	6	4
R3	0.8	1	4	2

Effect of the flow rate on the swimming velocity is studied for three different robots R1, R2, and R3, with the same dimensions except the tail lengths. Since the wavelength (helical pitch) is kept the same for all three robots, the number of waves, N_λ, are 6, 4 and 2 for R1, R2, and R3 respectively. Swimming velocities, U_{sw}, are plotted according to the rotation of the magnetic field in the **x-** direction for different flow rates (Figure 5.2).

Forward (backward) swimming is in the negative (positive) **x-** direction as shown in Figure 5.1. Positive (negative) rotation frequencies indicate counter-clock wise (CCW) (clock wise (CW)) rotation of the magnetic field for the swimmers with left-handed helical (LHH) tails. The swimmer moves against the flow for positive rotation frequencies, and in the direction of the flow for negative frequencies (Figure 5.1). Increasing flow rate decreases (increases) the swimming velocity in the forward (backward) direction. Swimming velocities vary linearly with the frequency of rotations up to about 20 Hz. For larger values of the rotation rate, swimmers cannot sustain synchronous rotation with the magnetic field, and velocities decrease rapidly.

Table 5.2. Reynolds numbers for different characteristic lengths. V_{flow} is the average velocity.

| | | | D_{head} | $D_{channel}$ |
| | | | $D = 0.8$ [mm] | $D = 1.6$ [mm] |
	μl/min	V_{flow} [mm/s]	Re_1	Re_2
Flow Rates	25	0.207	1.48E-05	2.96E-04
	50	0.414	2.96E-04	5.92E-04
	75	0.622	4.44E-04	8.88E-04

Average velocity of the flow, V_{flow}, is 0.207, 0.414 and 0.622 mm/s in the 1.6 mm-diameter channel for 25, 50 and 75 μl/min flow rates respectively. In Table 5.3, swimming velocities, U_{sw}, are presented for backward and forward swimming at 15 Hz for Robot R1 along with relative changes with respect to the no flow case. Since the forward (backward) swimming is in the opposite (same) direction of the channel flow (see Figure 5.1), the velocity of the swimmer decreases (increases) as the channel flow rate increases. Moreover, the rate of change in the swimming velocity is not proportional to the average velocity of the flow. The decrease in the forward velocity of the swimmer is by 1.14, 1.42 and 1.20 times the average velocity of the flow in the channel for flow rates equal to 25, 50 and 75 μl/min respectively. Similarly, the increase in the backward velocity is by 1.40, 1.67 and 1.58 times the average velocity of the flow for those flow rates.

Swimming behavior of R1, R2 and R3 is similar under the effect of constant flow rates (Figure 5.2). Due to tail length, R1 is the fastest and R3 is slowest robot under the same channel flow conditions. Swimmers cannot swim in the forward direction against the flow at low frequencies (1 - 3 Hz) in close proximity to the channel wall. Although

the swimmers continue to rotate at low frequencies with the applied rotating magnetic field, the swimmers are dragged in the backward direction with the effect of the flow for all flow rates. For positive rotation rates ($\omega_x/2\pi > 0$), positive swimming velocities ($U_{sw} > 0$) represent the drag velocities in Figure 5.2. Robot R1 can swim against flow after 5 Hz for all flow rates, whereas Robot R3 can swim against flow only for high frequencies (after 15 Hz) at 25 μl/min. Moreover swimming velocities show linear pattern according to rotation rates in the absence of the flow and for low flow rates, however linear pattern is fluctuating at high flow rates (50 and 75 μl/min in Figure 5.2).

Table 5.3. Flow effect on swimming velocity with respect to the average flow velocity (V_{flow}) for Robot R1.

Q [μl/min]	V_{flow} [mm/s]	Forward swimming		Backward swimming	
		U_{sw} at 15 Hz [mm/s]	$\dfrac{\left|U_{sw}\right|-\left|U_{sw,0}\right|}{V_{flow}}$	U_{sw} at 15 Hz [mm/s]	$\dfrac{\left|U_{sw}\right|-\left|U_{sw,0}\right|}{V_{flow}}$
0	0	-1.669	-	1.666	-
25	0.207	-1.432	**-1.14**	1.956	**1.40**
50	0.414	-1.080	**-1.42**	2.359	**1.67**
75	0.622	-0.925	**-1.20**	2.651	**1.58**
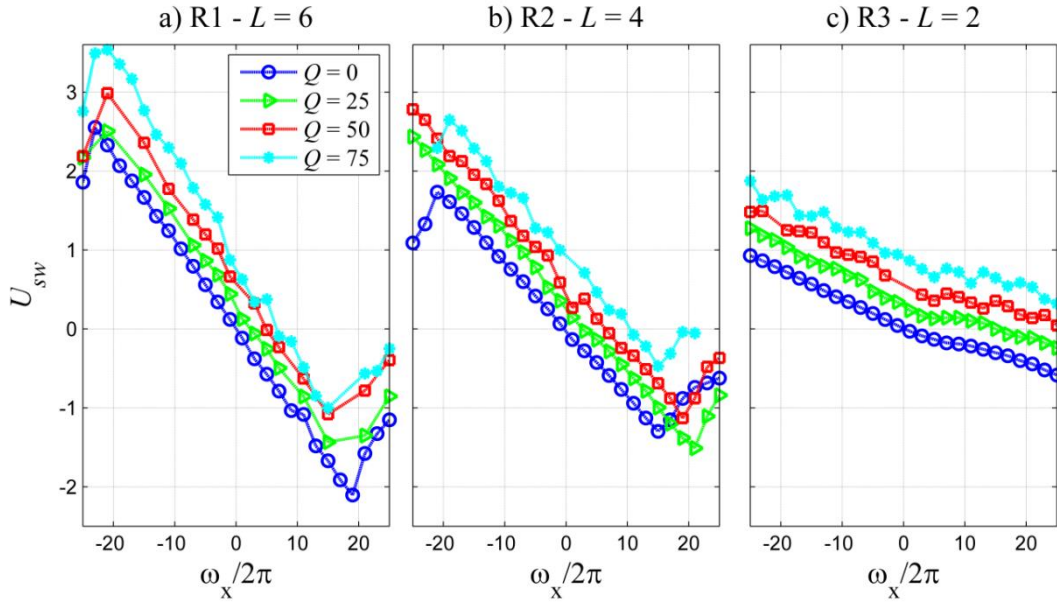
Figure 5.2 Swimming velocities, U_{sw} [mm/s], for Robot R1, R2 and R3 under effect of the fluid flow inside channel. Q [μl/min] is flow rate and ω_x is angular velocity about x-axis.

In Figure 5.3a comparison of data obtained from the simulation and experiments are depicted for different flow rates. For all flow rates, experiment results agree well with the center simulation results. After step-out frequency, swimming velocities are not predictable since the swimmers moves with an irregular pattern. Moreover, for forward motion of Robot R2, as flow rate is increased the step-out frequency also decreases. The step-out frequencies are 21, 19 and 15 for 25, 50 and 75 µl/min flow rates, respectively (Figure 5.3).
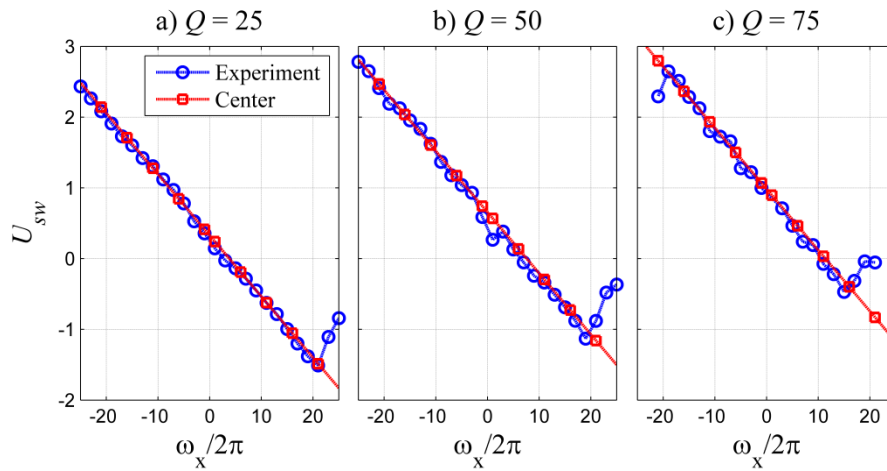
Figure 5.3 Comparison of experimental and simulation results in the channel center. The swimming velocities, U_{sw} [mm/s], of Robot R2 are represented for a) $Q = 25$ µl/min, b) $Q = 50$ µl/min, c) $Q = 75$ µl/min, where ω_x is angular velocity about **x**- axis.

5.1   Swimming Trajectories

Backward and forward motions of swimmer show different characteristics. In the forward motion, the swimmer follows helical trajectory; whereas it is a straight line for backward motion. Although fluid flow affects the swimmer velocity in both directions, it does not considerably affect the trajectory of the swimmer.

In Figure 5.4, swimmer trajectories at 15 Hz are represented in order to see the effect of the flow on swimmer trajectory. For all flow rates, the swimmer follows the helical trajectory in the forward motion. Although the amplitude of the helical trajectory does not vary considerably, the wavelength of the trajectory decreases as flow rate is increased (Figure 5.4). Wavelengths of the trajectories are approximately 0.6, 0.45, 0.3, 0.2 mm for 0, 25, 50, 75 µl/min respectively. Since the swimmer propels against the flow, for high flow rates, due to decrease in the U_{sw}, the wavelength of the helical trajectory decreases.
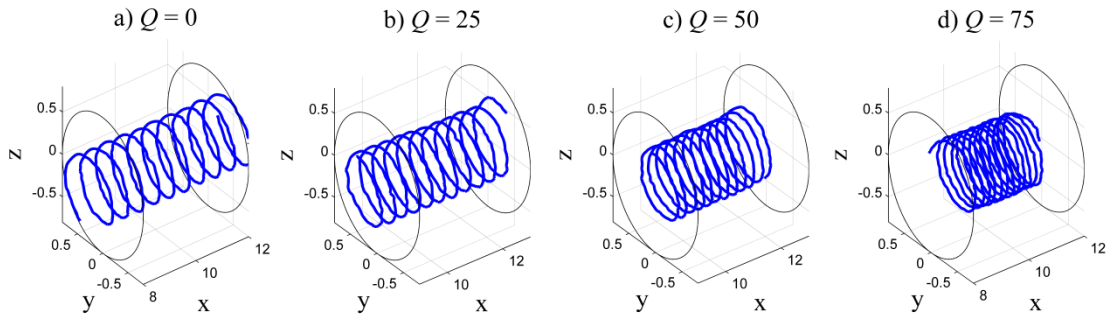
Figure 5.4 Swimmer trajectories for Robot R2 at 15 Hz for forward motion a) $Q = 0$ µl/min, b) $Q = 25$ µl/min, c) $Q = 50$ µl/min, d) $Q = 75$ µl/min. Q [µl/min] is flow rate in the channel. Units of **x**-, **y**- and **z**- axis are in millimeter [mm].

For backward motion, swimmer trajectories at 15 Hz are demonstrated in Figure 5.5. In backward motion, the swimmer propels in the tail direction (see Figure 5.1). The swimmer starts its motion with an oscillatory behavior. After 2 to 3 mm motion, the trajectory becomes stable in the channel center and the swimmer follows a straight line. In the case of constant flow, the amplitude of oscillations during the beginning of the motion is amplified with effect to the flow; the laminar flow profile delays the stabilization of motion in the channel center. As flow rate is increased, the maximum distance increases that the swimmer takes before it stabilizes its motion in the channel center (Figure 5.5a-d).
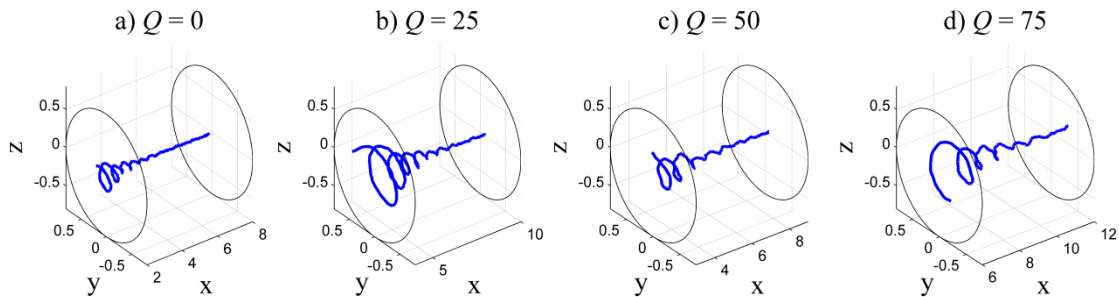
Figure 5.5 Swimmer trajectories for Robot R2 at 15 Hz for backward motion a) $Q = 0$ µl/min, b) $Q = 25$ µl/min, c) $Q = 50$ µl/min, d) $Q = 75$ µl/min.

Swimmer trajectories observed here are consistent with and complement previous studies on trajectories of low-Reynolds number swimmers in circular channels [41, 46, 60]. Berke et al. [60] used a point stresslet representation of a swimmer to study near wall trajectories and concluded that pusher type swimmers tend to follow trajectories parallel to the nearest surface, in effect, consistently with the helical trajectories observed in the experiments for in-channel swimming, where the attraction to the solid surface keeps the pusher near the channel wall at all times as shown in Figure 5.4. Zhu

et al. [46] studied spherical squirmers in circular channels and concluded that puller-type swimmers have wavelike trajectories that decrease in amplitude and converge to a stable trajectory parallel to the tube's axis as observed in Figure 5.5, whereas pushers are always unstable. Lastly, Zöttl & Stark [41] studied spherical squirmers in circular channels with Poiseuille flow and reported that pushers perform stable oscillations around the centerline of the channel with specific amplitude and hydrodynamic interactions with the channel wall stabilize the upstream orientation of the pullers. In our experiments tail pushes the swimmer in the upstream direction and pulls in the downstream. According to Figure 5.5, increasing channel flow rate leads to longer oscillations before the trajectory of the puller-type swimmer is stabilized indicating a destabilizing effect of the channel flow.

We conducted a number of additional simulations to obtain snap-shot solutions for the robot R2 at the centerline of the channel, near the channel wall, and by perturbing the orientation of the swimmer, which is parallel to the centerline of the channel, slightly. In all cases, steady-solutions to Stokes equations lead to symmetric linear and angular velocities as expected from the linearity of governing equations. When the swimmer (R2) is located 0.2 mm away from the channel wall and parallel to the centerline, the radial velocity is negative (-0.05 mm/s) when the tail rotates at 10 Hz and pushes the swimmer, and positive ($+0.05$ mm/s) consistent with the stability of backward swimming when the swimmer is pulled by the tail. Moreover, even when the swimmer is rotated slightly in the **y**-direction counter-clockwise by two degrees, $\delta\theta_y = +2^o$, so that the tail orients towards the wall, the radial velocity is still slightly negative (positive) when the tail pulls (pushes) the swimmer.

5.2   Channel & Flow Effect

Robot R2 which has four number of waves on its tail is used in these set of experiments. The swimmer's motion is observed in three different channels whose diameters are $D_{ch} = 1.6, 3, 4.8$ mm. Frequency dependent swimmer velocities are presented in Figure 5.6. Velocity profiles form a straight line in a narrow channel, whereas this regularity is not observed in the wider ones. Due to restriction, the swimmer moves faster in narrow channels than in the wide ones because of the increasing traction force in narrow channels as long as the magnetic torque high enough

to overcome the viscous torque. In the wide channels (D_{ch} = 3, 4.8 mm) the swimmer does not follow helical trajectory for all frequencies in the head direction but follows more complex trajectories.
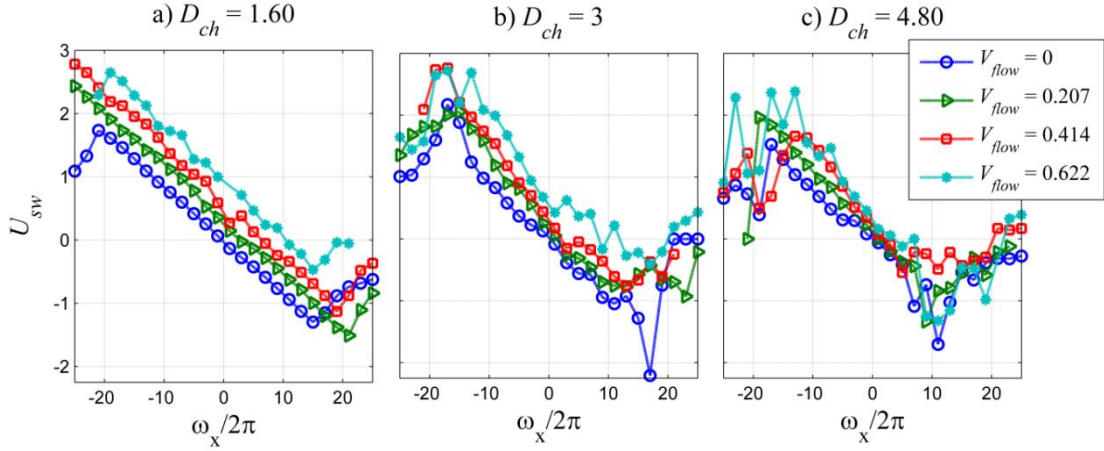
Figure 5.6 Flow effect in the circular channels whose diameters are a) D_{ch} = 1.6 mm, b) D_{ch} = 3 mm, c) D_{ch} = 4.8 mm, for flow velocities are V_{flow} = 0, 0.207, 0.414, 0.622 mm/s.

In Figure 5.7a-f, swimming velocities from experiments (blue lines with circles) are compared with the ones from simulations for the case when the robot is placed at the center of the channel (green lines with squares) and 0.1 mm away from the channel wall (red lines with squares). The effect of the radial position on the swimming velocity is different for each channel. Typically, the swimming speed improves with the radial position of the robot gradually reaching to a maximum first then rapidly goes to zero due to the stiction constraint when the robot touches the wall [40]. In experiments, the swimmer is very close to the channel wall due to gravity, especially when stationary. Thus, the distance of the swimmer from the wall is fixed at a numerically feasible minimum value in near-wall simulations for all channels.

When there is no flow in the channel, simulations for the robot placed at the centerline of the 1.6-mm diameter channel agree very well with the experiments (Figure 5.7a) indicating that the robot travels near the center of the channel. Near-wall swimming speeds in this case are about 30% larger than centerline speeds.

For the channel with 3.0-mm diameter, swimming velocities for the centerline and near-wall simulations are very close to each other and to experimental results (Figure 5.7b). Near-wall swimming speeds are slightly larger than the center swimming and agree with experimental results at high rotation rates in the forward and the backward directions, when there is no flow in the channel.

For the channel with the largest diameter, experimental results and simulations agree better for forward swimming than the backward swimming case, when there is no flow (Figure 5.7c). According simulations to centerline and near-wall swimming speeds are very close for this channel as well. Discrepancy for backward swimming results can be due to the orientation of the swimmer, which is taken as parallel to the channel's axis (**x**-direction) in simulations, but may differ in experiments especially in larger diameter channels as there is more room for the swimmer to find an equilibrium position and orientation under the effects of hydrodynamic interactions. Further experiments are necessary to determine the orientation and the position of the swimmer.
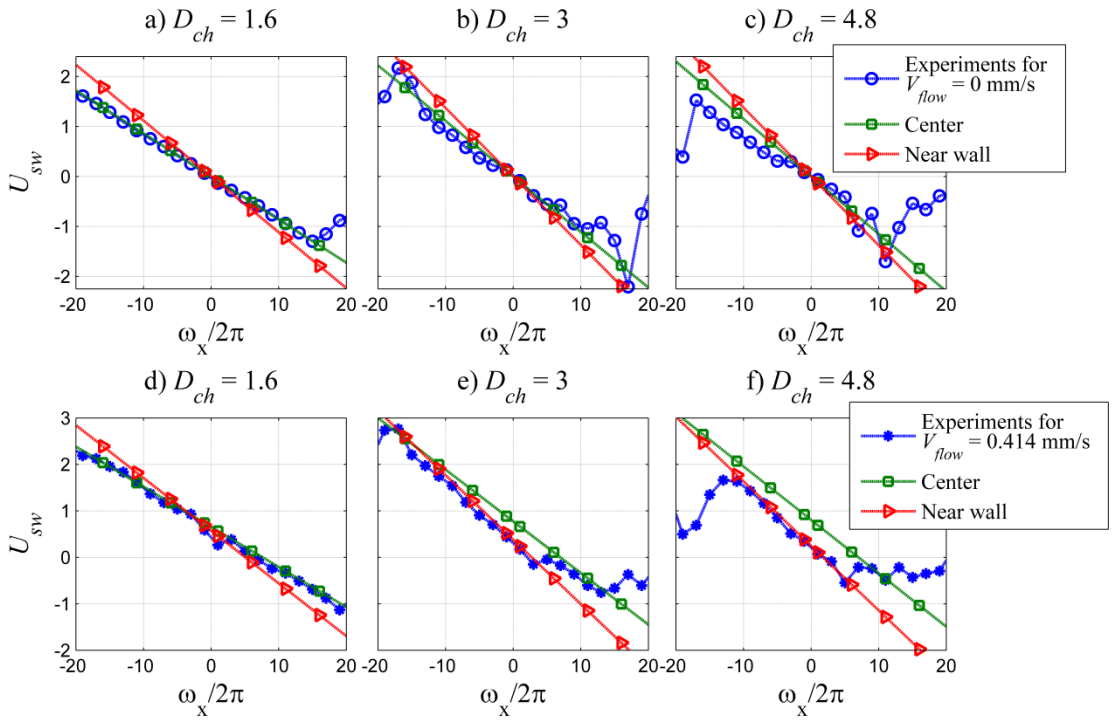
Figure 5.7 Simulation and experiment comparison for different channel diameter and average flow velocities.($V_{flow} = 0$ mm/s for (a, b, c) and $V_{flow} = 0.414$ mm/s for (d, e, f)).

In Figure 5.7d-f, swimming velocities from simulations are compared to measurements from experiments when there is a Poiseuille flow with an average velocity of 0.414 mm/s in all channels. Similarly to the case when there is no flow in the 1.6-mm diameter channel, the swimming velocities from simulations for the robot at the centerline of the channel agree very well with experiments in Figure 5.7d.

For the 3.0-mm channel, swimming speeds from simulations and experiments agree very well for effective forward swimming, when $U_{sw} < 0$ and $\omega_x/2\pi > 5$ Hz, and for backward swimming when the clockwise rotation rate is high ($-\omega_x/2\pi > 10$ Hz). According to experiments, swimming conditions for $-5 < \omega_x/2\pi < 5$ Hz indicate that the

swimmer is not aligned with the channel's axis (Figure 5.7e). In experiments, the swimmer makes a wobbling motion about the **x**-direction that coincides with the channel's axis for $-5 < \omega_x/2\pi < 5$ Hz. For $\omega_x/2\pi < -5$ Hz (backward motion), the swimmer is aligned with **x**-axis up to the step-out frequency.
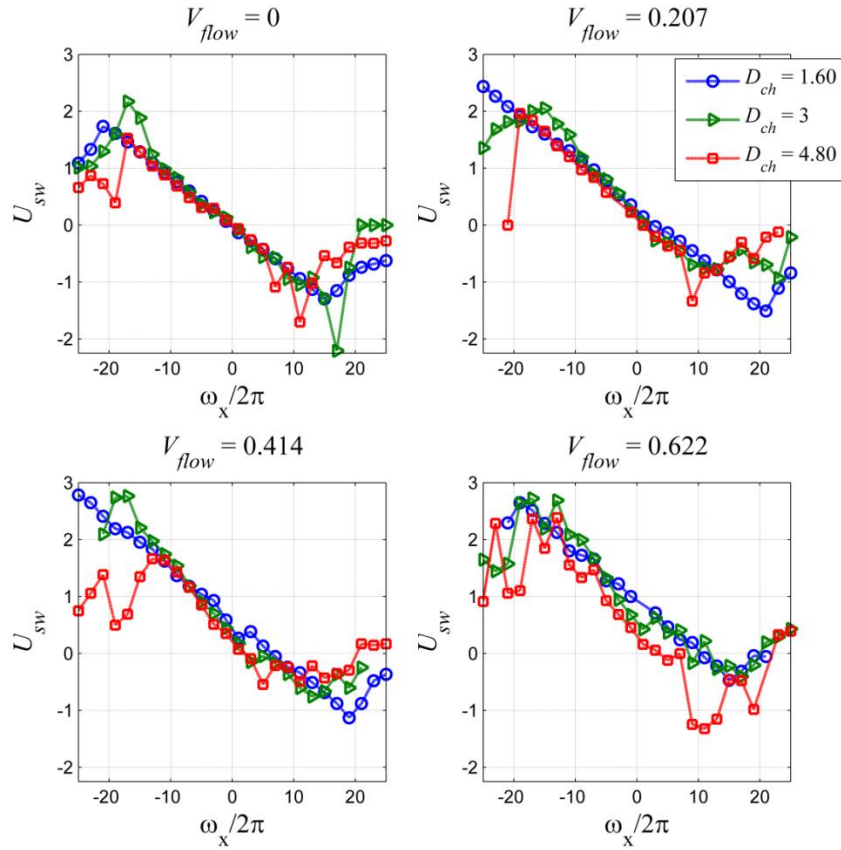
Figure 5.8 Swimming velocity [Usw, mm/s] – rotation rates [$\omega x/2\pi$, 1/s] plots for flow velocities a) Vflow = 0 mm/s, b) 0.207 mm/s, c) 0.414 mm/s, d) 0.622 mm/s in three different channels.

Lastly, for $D_{ch} = 4.8$ mm, the swimming speed is highly irregular at high rotation rates in the forward ($\omega_x/2\pi > 5$ Hz) and the backward ($-\omega_x/2\pi > 10$ Hz) directions in the case of Poiseuille flow in the channel with the average velocity of 0.414 mm/s (Figure 5.7f). Simulation results for near-wall swimming agree significantly better with experimental measurements than the simulations for center-swimming when the swimming speed is proportional to the rotation rate. Moreover, overall results demonstrate that the robot swims in narrower channels at higher effective speeds than wider channels partly due to increasingly irregular even "chaotic" swimming patters as reported by Chacón [42]. Confinement in narrow channels improves the regularity of swimming and hence allows higher swimming speeds.

We also observed the channel effect under fix flow rate (Figure 5.8). In the absence of the flow, the swimming velocities, U_{sw}, follow same trend in different channels up to step-out frequency; the velocity profiles have same slope which remains unchanged as the channel diameter is increased (Figure 5.8a). As the flow is introduced to the channel (at V_{flow} = 0.207 mm/s), Robot R2 has higher backward velocities after 10 Hz up to step-out frequency in the channel with D_{ch} = 3 (Figure 5.8b). As the average flow velocity is increased to 0.414 mm/s, backward velocities for D_{ch} = 4.8 follow same trend with the other channels whereas the decrease in forward velocity is higher than the other ones (Figure 5.8c). For V_{flow} = 0.622 mm/s, velocity profile of Robot R2 shows an oscillating behavior in the channel with D_{ch} = 4.8 (Figure 5.8d). Moreover the magnitudes of the velocities for the backward motion are lower in the wide channel (Figure 5.8d). Presence of a flow inside the channels has a more pronounced effect on the swimmer velocity in wider channels. For all cases, after step-out frequency, swimmer velocities are not predictable; show an irregular pattern.

6   CONCLUSION

Low Reynolds number swimming of an artificial structure that consists of a cylindrical body and a rigid helical tail is modeled with the three-dimensional CFD model here. Effects of the radial position of the swimmer, length and radius of the cylindrical body, number and amplitude of helical waves on the linear and angular velocities of the swimmer are studied using the model. According to results, as the distance between channel wall and the swimmer decreases, forward velocity increases due to traction forces. The number of helical turns on the tail of the swimmer placed near the channel wall improves the magnitude of the forward velocity of the swimmer between one and four helical turns in the tail. Swimming speed also increases with the radius of the body and the helical tail of the swimmer for up to a value that corresponds to $3/5^{th}$ of the channel radius, then decreases due to increasing drag force on the swimmer. Increasing the length of the cylindrical body of the swimmer affects the flow induced by the rotation of the swimmer, thus, increases the velocity of the swimmer in the tangent-direction with respect to the channel wall, and decreases the forward velocity of the swimmer. Our experiments are underway to validate the CFD model and characterize the behavior of swimmers with cylindrical bodies.

In this thesis, the 3D finite element method (FEM) based simulations of microswimmers with cylindrical magnetic head and helical tail are conducted and corresponding experimental studies are performed for the same cases in order to validate numerical works. Regarding the design of microswimmers to propel in low Reynolds numbers, there are many aspects to be elucidated that affect the swimming efficiency such as swimmer geometry, fluid medium and confinement geometry. In this study, swimmer velocities are presented by changing the swimmer and confinement geometry where fluid in all cases is glycerol so as to find the individual effects of all parameters. Moreover, external flows with constant rate are introduced to the channel to confirm that microswimmers can be controlled against fluid flow. Fluid flow effect on swimmer trajectories is also represented. Moreover channel radius effect is also

observed and we report that confinement leads to more stable trajectories compared to the ones in wide channels. Generally, swimmers follow helical trajectory in the head direction (forward motion), which is also observed in bacteria motion. Stable straight trajectories are also for various swimmer geometries in the tail direction (backward motion). Effects of the helical wavelength of the tail and tail length on swimming velocities are discussed with experimental and numerical studies. At constant tail length, there is an optimal wavelength which maximizes the swimming velocity. Furthermore, longer tails provide faster forward and backward motion for fixed wavelength.

CFD simulations are performed to compare experimental results. In each case, swimmer geometries used in experiments are modeled; for low Reynolds number swimming of microswimmers, Stokes equations are computed. Our simulation results are in very good agreement with the experimental results.

A CFD model is developed to analyze the swimming of singly-flagellated bacteria with a spheroid head in circular channels. Force- and torque-free swimming conditions are used in the model to obtain forward and lateral velocities and rotation rates of model organisms. Linear and angular velocities of the organism and swimming efficiencies are computed with the CFD model for varying tail length, wavelength, channel radius and the tail radius. Maximum forward velocity is obtained for $\lambda/s = 3$ and $L/s = 8$ in both the large channel that mimics free-swimming conditions and the channel with a radius three times the short axis of the spheroid head. The maximum efficiency is obtained for $\lambda/s = 4$ and $L/s = 8$ in the narrow channel, but for $\lambda/s = 3$ and $L/s = 4$ in the large one. Unless inside narrow channels, for which $R_{ch}/r < 3$, the forward velocity does not vary significantly, but decreases sharply to almost zero for $R_{ch}/r \approx 1.5$. However, the swimming efficiency is almost twice as much in narrow channels with $R_{ch}/r \approx 3$ as the one in large channels $R_{ch}/r > 10$.

For integer number of waves on the tail, the magnitude of the lateral motion attains maximum values, whereas for number of waves, 1.5, 2.5, 3.5, the magnitude becomes minimum because of the envelope growth of the amplitude near the joint. In principle, magnitude of lateral velocities depends on the completion of helical turns that ensures the symmetry of the helix, however the smooth ramp-up of the helical radius near the joint, which connects the body and the tail, breaks the symmetry. Moreover, the lateral motion and wobbling rate, which is the magnitude of rotation rates of the cell in

perpendicular directions to its motion, are suppressed as the radius of the channel decreases, consistent with the observations in literature.

Lastly, the effect of the tail radius is also characterized in conjunction with the effects of the tail length and the channel radius. As the radius of tail is increased, there is a critical channel radius the velocity and the efficiency of the swimmer are maximized. The normalized critical channel radius, R_{ch}/r, varies between 2 and 3 depending on the length and the radius of the tail. The forward velocity and the efficiency are higher for thicker tails in narrow channels than thinner tails, and vice versa in wide channels.

This thesis will contribute to literature by shedding light on the swimming behavior of bacteria-like microswimmers confined in circular geometries, which have the potential to be used in important biomedical applications such as minimally invasive surgeries, drug delivery systems and opening clogged arteries.

6.1   Future Work

In order to practice microswimmers in biomedical applications in human body, motion of microswimmer should be studied further. Microswimmer motion in flexible channels can be studied as future work. Here, swimmers with rigid helical tail are presented; second step might be investigating the swimmer behavior with flexible tail which will be manufactured with different process other than 3D printer. Also in this thesis swimmer velocity and trajectory are obtained with image processing tools. Using velocity and trajectory information from the recorded videos as feedback, closed-loop control can be performed for real-time trajectory control of swimmers. Instead of images and recorded videos, information obtained from magnetic sensors can be used as feedback for control algorithm. Once a control mechanism is developed, experiments in living tissue can be performed as future work.

APPENDIX: IMAGE PROCESSING CODE IN MATLAB

In order to obtain velocities and trajectory of the swimmer from the recorded video files, a MATLAB code is written which detects black head of the swimmer.

Inputs of the function are *n* (video name without extension), *angle* (rotation angle of image), *fps* (frame per second of the recorded video), *threshold* (black color intensity) and *rect* (rectangle sizes for crop operation). Outputs of the function are U_{sw} (swimming velocity of the swimmer) and the coordinates of the trajectory (*x* and *y*).

The code performs following tasks sequentially. First of all, the video is read and each frame is written in a matrix (*frames*). Since video images have irrelevant parts, only the region that swimmer is moving is cropped; the width of the cropped image is 20 mm defined with the graph paper. If the long axis of the channel is not horizontal in the screen, it is rotated by an amount of *angle* degree. *angle* is generally not more than ±2°. Than channel boundaries are highlighted with solid color (blue). This code is written to detect black parts in the image; thus head of the swimmers are dyed to black. The code defines the centroid of the black parts. In each frame, coordinates of the centroids are recorded where units are pixel. Unit of the coordinates are converted to millimeter (mm) with the aid of the cropped image width. At the same time cropped images are recorded to a new video with video writer function. The trajectory of the swimmer is plotted to a figure using coordinates of the centroids in mm. Lastly, the code saves the figure as '.fig' file and trajectory coordinates as '.mat' file.

```matlab
function [Usw,x,y] = top(n,angle,fps,threshold,rect)
%% --------------------------SAMPLE-INPUTS------------------------%
% n=15;                   % name of the video .mp4 , n is frequency.
% angle= 0;               % rotation angle of image
% fps = 120;              % frames per second
% threshold = .75;        % threshold is determined experimentally
% Top view adjustment with rectangular crop
% rect = [xmin ymin width height] ; % in pixels
% rect = [364 217 150 28];
upl = 20/rect(1,3);       % unit pixel length [mm/pixel]
%% video name
string1 = ['' num2str(n) '.mp4'];
%% to access the video and get basic information about it
swimmerObj = VideoReader(string1);
```

```matlab
%% get frames from video
frames = read(swimmerObj);
%% Select region where swimmer is moving
nFrames = size(frames,4); % Number of frames
first_frame = frames(:,:,:,1);
first_region = imcrop(first_frame,rect);
frame_regions = repmat(uint8(0), [size(first_region) nFrames]);
for count = 1:nFrames
frame_regions(:,:,:,count) =
imcrop(imrotate(frames(:,:,:,count),angle),rect);
% define channel boundaries
y1=2;  % in pixels upper bound of the channel
frame_regions(y1,:,1,count)=0;
frame_regions(y1,:,2,count)=0;
frame_regions(y1,:,3,count)=255;
y2=27; % in pixels upper bound of the channel
frame_regions(y2,:,1,count)=0;
frame_regions(y2,:,2,count)=0;
frame_regions(y2,:,3,count)=255;
end

%%
seg_sw = false([size(first_region,1) size(first_region,2) nFrames]);
centroids = zeros(nFrames,2);
se_disk = strel('disk',1);
%%
for count = 1: nFrames
    fr = frame_regions(:,:,:,count);
    gfr = rgb2gray(fr);
    gfr = imcomplement(gfr);
    bw = im2bw(gfr,threshold);  % threshold is determined
experimentally
    bw = imopen(bw,se_disk);
    bw = imclearborder(bw);
    seg_sw(:,:,count) = bw;
end
%% Use |regionprops| to calculate the center of the swimmer head.
sw_centers = zeros(nFrames,2);
for count = 1:nFrames
    property = regionprops(seg_sw(:,:,count), {'Centroid','Area'});
    AA = [property.Centroid];
    TF = isempty(AA);
    if TF == 1
        sw_centers(count,:) = [0,0];
    else
        sw_centers(count,1) = AA(1,1);
        sw_centers(count,2) = AA(1,2);
    end
    if ~isempty([property.Area])
        areaArray = [property.Area];
        [junk,idx] = max(areaArray);
        c = property(idx).Centroid;
        c = floor(fliplr(c));
        width = 0;
        row(count) = c(1)-width:c(1)+width;
        col(count) = c(2)-width:c(2)+width;
        r = [ 255 255 0 ];
        frame_regions(row(count),col(count),1,count) = r(1);% red
        frame_regions(row(count),col(count),2,count) = r(3);% green
        frame_regions(row(count),col(count),3,count) = r(3);% blue
    end
```

```matlab
%to draw trajectory with yellow line on video
            if count>1
                for nc = 1:1:count-1
                    frame_regions(row(nc),col(nc),1,count) = r(1);%
red
                    frame_regions(row(nc),col(nc),2,count) = r(2);%
green
                    frame_regions(row(nc),col(nc),3,count) = r(3);%
blue
                end
            end
end
%%  writing frames as avi file
% Play video
implay(frame_regions,100);
%% Write video
string133 = ['' num2str(n) '.avi']; % video name
writerObj = VideoWriter(string133);
writerObj.FrameRate = 100;
open(writerObj);
writeVideo(writerObj,frame_regions);
close(writerObj);
%% Display Swimmer centers in mm
x = sw_centers(:,1);
y = sw_centers(:,2);
%
N = max(size(x));
cc = mean(y);
% Unit conversion
x  = x * upl;
y  = (y-cc) * upl;
% in order to calcutale average forward velocity Usw
Usw = ((x(nFrames)-x(1))/(nFrames-1))*fps;  % mm/sec
figure (1)
plot(x,y,'r.',...
    'LineWidth',2); grid on
% legend('trajectory','smooth trajectory','upper channel wall','lower
channel wall')
xlabel('x [mm]'); ylabel('y [mm]'); zlabel('z');
str1 = sprintf('Swimming trajectory and U_{sw} = %f mm/s - %d
Hz',Usw,n);
title(str1);
string10 = ['top_view_' num2str(n) '.fig'];
hgsave(string10);
str13 = ['top_view_' num2str(n) '.mat'];
save(str13,'x','y');
```

REFERENCES

[1]   Ghosh, A., & Fischer, P. (2009). Controlled propulsion of artificial magnetic nanostructured propellers. *Nano letters*, *9*(6), 2243-2245.

[2]   Tottori, S., Zhang, L., Peyer, K. E., & Nelson, B. J. (2013). Assembly, disassembly, and anomalous propulsion of microscopic helices. *Nano letters*,*13*(9), 4263-4268.

[3]   Martel, S., Mohammadi, M., Felfoul, O., Lu, Z., & Pouponneau, P. (2009). Flagellated magnetotactic bacteria as controlled MRI-trackable propulsion and steering systems for medical nanorobots operating in the human microvasculature. *The International journal of robotics research*, *28*(4), 571-582.

[4]   Shum, H., Gaffney, E. A., & Smith, D. J. (2010). Modelling bacterial behaviour close to a no-slip plane boundary: the influence of bacterial geometry.*Proceedings of the Royal Society A: Mathematical, Physical and Engineering Science*, rspa20090520.

[5]   Goto, T., Masuda, S., Terada, K., & Takano, Y. (2001). Comparison between observation and boundary element analysis of bacterium swimming motion.*JSME International Journal Series C*, *44*(4), 958-963.

[6]   Dreyfus, R., Baudry, J., Roper, M. L., Fermigier, M., Stone, H. A., & Bibette, J. (2005). Microscopic artificial swimmers. *Nature*, *437*(7060), 862-865.

[7]   Abbott, J. J., Lagomarsino, M. C., Zhang, L., Dong, L., & Nelson, B. J. (2009). How should microrobots swim? *The International Journal of Robotics Research*.

[8]   Zhang, L., Abbott, J. J., Dong, L., Kratochvil, B. E., Bell, D., & Nelson, B. J. (2009). Artificial bacterial flagella: Fabrication and magnetic control. *Applied Physics Letters*, *94*(6), 064107.

[9]   Honda, T., Arai, K. I., & Ishiyama, K. (1996). Micro swimming mechanisms propelled by external magnetic fields. *Magnetics, IEEE Transactions on*, *32*(5), 5085-5087.

[10]   Tabak, A. F., & Yesilyurt, S. (2012, June). Experiments on in-channel swimming of an untethered biomimetic robot with different helical tails. In*Biomedical Robotics and Biomechatronics (BioRob), 2012 4th IEEE RAS & EMBS International Conference on* (pp. 556-561). IEEE.

[11]   Hancock, G. J. (1953). The self-propulsion of microscopic organisms through liquids. *Proceedings of the Royal Society of London. Series A. Mathematical and Physical Sciences*, *217*(1128), 96-121.

[12]   Gray, J., & Hancock, G. J. (1955). The propulsion of sea-urchin spermatozoa. *Journal of Experimental Biology*, *32*(4), 802-814.

[13]   Temel, F. Z., & Yesilyurt, S. (2011, April). Magnetically actuated micro swimming of bio-inspired robots in mini channels. In *Mechatronics (ICM), 2011 IEEE International Conference on* (pp. 342-347). IEEE.

[14]   Tabak, A. F., Temel, F. Z., & Yesilyurt, S. (2011, September). Comparison on experimental and numerical results for helical swimmers inside channels. In *Intelligent Robots and Systems (IROS), 2011 IEEE/RSJ International Conference on* (pp. 463-468). IEEE.

[15]   Biondi, S. A., Quinn, J. A., & Goldfine, H. (1998). Random motility of swimming bacteria in restricted geometries. *AIChE journal*, *44*(8), 1923-1929.

[16]   Berg, H. C., & Turner, L. (1990). Chemotaxis of bacteria in glass capillary arrays. Escherichia coli, motility, microchannel plate, and light scattering.*Biophysical Journal*, *58*(4), 919-930.

[17]   Liu, Z., & Papadopoulos, K. D. (1996). A method for measuring bacterial chemotaxis parameters in a microcapillary. *Biotechnology and bioengineering*,*51*(1), 120-125.

[18]   Nogueiral, F. S., & de Barros, H. G. L. (1995). Study of the motion of magnetotactic bacteria. *European biophysics journal*, *24*(1), 13-21.

[19]   Zeile, W. L., Zhang, F., Dickinson, R. B., & Purich, D. L. (2005). Listeria's right-handed helical rocket-tail trajectories: Mechanistic implications for force generation in actin-based motility. *Cell motility and the cytoskeleton*, *60*(2), 121-128.

[20]   Dickinson, R. B., Caro, L., & Purich, D. L. (2004). Force generation by cytoskeletal filament end-tracking proteins. *Biophysical journal*, *87*(4), 2838-2854.

[21]   Crenshaw, H. C. (1996). A new look at locomotion in microorganisms: rotating and translating. *American zoologist*, *36*(6), 608-618.

[22]   Segel, L. A. (1984). Taxes in cellular ecology. In *Mathematical Ecology* (pp. 407-424). Springer Berlin Heidelberg.

[23]   Armitage, J. P. (1999). Bacterial tactic responses. *Advances in microbial physiology*, *41*, 229-289.

[24]   Berg, H. C. (2003). The rotary motor of bacterial flagella. *Biochemistry*, *72*(1), 19.

[25]   Li, G., Tam, L. K., & Tang, J. X. (2008). Amplified effect of Brownian motion in bacterial near-surface swimming. *Proceedings of the National Academy of Sciences*, *105*(47), 18355-18359.

[26]   DiLuzio, W. R., Turner, L., Mayer, M., Garstecki, P., Weibel, D. B., Berg, H. C., & Whitesides, G. M. (2005). Escherichia coli swim on the right-hand side.*Nature*, *435*(7046), 1271-1274.

[27]   Kantsler, V., Dunkel, J., Polin, M., & Goldstein, R. E. (2013). Ciliary contact interactions dominate surface scattering of swimming

eukaryotes. *Proceedings of the National Academy of Sciences*, *110*(4), 1187-1192.

[28]   Männik, J., Driessen, R., Galajda, P., Keymer, J. E., & Dekker, C. (2009). Bacterial growth and motility in sub-micron constrictions. *Proceedings of the National Academy of Sciences*, *106*(35), 14861-14866.

[29]   Tabak, A. F., & Yesilyurt, S. (2010, January). Validated reduced order models for simulating trajectories of bio-inspired artificial micro-swimmers. In *ASME 2010 8th International Conference on Nanochannels, Microchannels, and Minichannels collocated with 3rd Joint US-European Fluids Engineering Summer Meeting* (pp. 57-63). American Society of Mechanical Engineers.

[30]   Temel, F. Z., & Yesilyurt, S. (2013). Simulation-based analysis of micro-robots swimming at the center and near the wall of circular mini-channels. *Microfluidics and nanofluidics*, *14*(1-2), 287-298.

[31]   Ramia, M., Tullock, D. L., & Phan-Thien, N. (1993). The role of hydrodynamic interaction in the locomotion of microorganisms. *Biophysical Journal*, *65*(2), 755-778.

[32]   Goto, T., Nakata, K., Baba, K., Nishimura, M., & Magariyama, Y. (2005). A fluid-dynamic interpretation of the asymmetric motion of singly flagellated bacteria swimming close to a boundary. *Biophysical journal*, *89*(6), 3771-3779.

[33]   Giacché, D., Ishikawa, T., & Yamaguchi, T. (2010). Hydrodynamic entrapment of bacteria swimming near a solid surface. *Physical Review E*, *82*(5), 056309.

[34]   Felderhof, B. U. (2010). Swimming at low Reynolds number of a cylindrical body in a circular tube. *Physics of Fluids (1994-present)*, *22*(11), 113604.

[35]   Lighthill, J. (1976). Flagellar hydrodynamics. *SIAM review*, *18*(2), 161-230.

[36]   Phan-Thien, N., Tran-Cong, T., & Ramia, M. (1987). A boundary-element analysis of flagellar propulsion. *Journal of Fluid Mechanics*, *184*, 533-549.

[37]   Lauga, E., DiLuzio, W. R., Whitesides, G. M., & Stone, H. A. (2006). Swimming in circles: motion of bacteria near solid boundaries. *Biophysical journal*, *90*(2), 400-412.

[38]   Higdon, J. J. L. (1979). The hydrodynamics of flagellar propulsion: helical waves.*Journal of Fluid Mechanics*, *94*(02), 331-351.

[39]   Keaveny, E. E., & Maxey, M. R. (2008). Spiral swimming of an artificial micro-swimmer. *Journal of Fluid Mechanics*, *598*, 293-319.

[40]   Acemoglu, A., & Yesilyurt, S. (2014). Effects of Geometric Parameters on Swimming of Micro Organisms with Single Helical Flagellum in Circular Channels. *Biophysical journal*, *106*(7), 1537-1547.

[41]   Zöttl, A., & Stark, H. (2012). Nonlinear dynamics of a microswimmer in Poiseuille flow. *Physical review letters*, *108*(21), 218104.

[42]   Chacón, R. (2013). Chaotic dynamics of a microswimmer in Poiseuille

flow. *Physical Review E*, *88*(5), 052905.

[43]   Uppaluri, S., Heddergott, N., Stellamanns, E., Herminghaus, S., Zöttl, A., Stark, H., ... & Pfohl, T. (2012). Flow Loading Induces Oscillatory Trajectories in a Bloodstream Parasite. *Biophysical journal*, *103*(6), 1162-1169.

[44]   Costanzo, A., Di Leonardo, R., Ruocco, G., & Angelani, L. (2012). Transport of self-propelling bacteria in micro-channel flow. *Journal of Physics: Condensed Matter*, *24*(6), 065101.

[45]   Wang, S., & Ardekani, A. M. (2012). Unsteady swimming of small organisms. *Journal of Fluid Mechanics*, *702*, 286-297.

[46]   Zhu, L., Lauga, E., & Brandt, L. (2013). Low-Reynolds-number swimming in a capillary tube. *Journal of Fluid Mechanics*, *726*, 285-311.

[47]   Purcell, E. M. (1977). Life at low Reynolds number. *Am. J. Phys*, *45*(1), 3-11.

[48]   Liu, Z., & Papadopoulos, K. D. (1995). Unidirectional motility of Escherichia coli in restrictive capillaries. *Applied and environmental microbiology*, *61*(10), 3567-3572.

[49]   Happel, J., & Brenner, H. (Eds.). (1983). *Low Reynolds number hydrodynamics: with special applications to particulate media* (Vol. 1). Springer.

[50]   Acemoglu, A., Temel, F. Z., & Yesilyurt, S. (2013, June). Characterization and modeling of microswimmers with helical tails and cylindrical heads inside circular channels. In *ASME 2013 11th International Conference on Nanochannels, Microchannels, and Minichannels* (pp. V001T12A005-V001T12A005). American Society of Mechanical Engineers.

[51]   Tabak, AF.; Yesilyurt, S. (2014). Improved Kinematic Models for Two-Link Helical Micro/Nanoswimmers, *Robotics, IEEE Transactions on*, vol.30, no.1, pp.14,25, Feb. 2014 doi: 10.1109/TRO.2013.2281551

[52]   Crenshaw, H. C., Ciampaglio, C. N., & McHenry, M. A. T. T. H. E. W. (2000). Analysis of the three-dimensional trajectories of organisms: estimates of velocity, curvature and torsion from positional information. *Journal of Experimental Biology*, *203*(6), 961-982.

[53]   Berg, H. C. (Ed.). (1993). *Random walks in biology*. Princeton University Press.

[54]   Peyer, K. E., Zhang, L., Kratochvil, B. E., & Nelson, B. J. (2010, May). Non-ideal swimming of artificial bacterial flagella near a surface. In *Robotics and Automation (ICRA), 2010 IEEE International Conference on* (pp. 96-101). IEEE.

[55]   Man, Y., & Lauga, E. (2013). The wobbling-to-swimming transition of rotated helices. *Physics of Fluids (1994-present)*, *25*(7), 071904.

[56]   Chattopadhyay, S., & Wu, X. L. (2009). The effect of long-range hydrodynamic interaction on the swimming of a single bacterium. *Biophysical journal*, *96*(5), 2023-2028.

[57]   Tabak, A. F., & Yesilyurt, S. (2013). Hydrodynamic surrogate models for bio-inspired micro-swimming robots. *arXiv preprint arXiv:1311.3429*.

[58]   COMSOL AB, Comsol Multiphysics User's Guide, 2012.

[59]   Kim, S., & Karrila, S. J. (2013). *Microhydrodynamics: principles and selected applications*. Courier Dover Publications.

[60]   Berke, A. P., Turner, L., Berg, H. C., & Lauga, E. (2008). Hydrodynamic attraction of swimming microorganisms by surfaces. *Physical Review Letters*,*101*(3), 038102.